ACS APPLIED MATERIALS & INTERFACES
Research Article
Cite This: ACS Appl. Mater. Interfaces 2019, 11, 25483−25494
www.acsami.org

Downloaded via UNIV OF SAO PAULO on July 22, 2019 at 14:02:20 (UTC).
See https://pubs.acs.org/sharingguidelines for options on how to legitimately share published articles.

Visible-Light-Mediated Photodynamic Water Disinfection @ Bimetallic-Doped Hybrid Clay Nanocomposites

Chidinma G. Ugwuja,[†,‡] Olawale O. Adelowo,[§] Aemere Ogunlaja,[†,∥] Martins O. Omorogie,[†,‡] Olumide D. Olukanni,[†,‡] Odion O. Ikhimiukor,[§] Ievgeniia Iermak,[⊥] Gabriel A. Kolawole,[†,‡,#] Christina Guenter,[□] Andreas Taubert,[○] Olusola Bodede,[△] Roshila Moodley,[△] Natalia M. Inada,[⊥] Andrea S.S. de Camargo,[⊥] and Emmanuel I. Unuabonah[*,†,‡,⊥]

[†]African Centre of Excellence for Water and Environment Research (ACEWATER), [‡]Department of Chemical Sciences, [∥]Department of Biological Sciences, Redeemer's University, PMB 230, Ede, Osun State 220005, Nigeria

[§]Department of Microbiology, University of Ibadan, PMB 5116, Ibadan, Oyo State 200284, Nigeria

[⊥]São Carlos Institute of Physics, University of São Paulo, Avenida Trabalhador Sãocarlense 400, São Carlos 13566-590, Brazil

[#]Department of Chemistry, University of Zululand, Kwadlangezwa, 3886, Republic of South Africa

[□]Institute of Geosciences, [○]Institute of ChemistryUniversity of Potsdam, Potsdam D-14476, Germany

[△]School of Chemistry and Physics, University of KwaZulu-Natal, Westville Campus, Durban, 3630, South Africa

Supporting Information

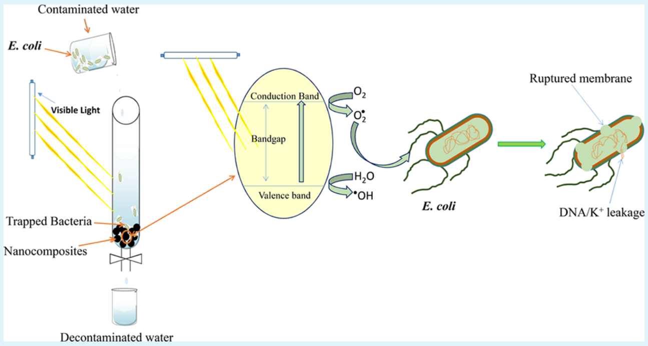

ABSTRACT: This study reports a new class of photocatalytic hybrid clay nanocomposites prepared from low-cost sources (kaolinite clay and *Carica papaya* seeds) doped with Zn and Cu salts via a solvothermal process. X-ray diffraction analysis suggests that Cu-doping and Cu/Zn-doping introduce new phases into the crystalline structure of Kaolinite clay, which is linked to the reduced band gap of kaolinite from typically between 4.9 and 8.2 eV to 2.69 eV for Cu-doped and 1.5 eV for Cu/Zn hybrid clay nanocomposites (Nisar, J.; Århammar, C.; Jämstorp, E.; Ahuja, R. *Phys. Rev. B* **2011**, *84*, 075120). In the presence of solar light irradiation, Cu- and Cu/Zn-doped nanocomposites facilitate the electron−hole pair separation. This promotes the generation of singlet oxygen which in turn improves the water disinfection efficiencies of these novel nanocomposite materials. The nanocomposite materials were further characterized using high-resolution scanning electron microscopy, fluorimetry, thermogravimetric analysis, and Raman spectroscopy. The breakthrough times of the nanocomposites for a fixed bed mode of disinfection of water contaminated with 2.32×10^7 cfu/mL *E. coli* ATCC 25922 under solar light irradiation are 25 h for Zn-doped, 30 h for Cu-doped, and 35 h for Cu/Zn-doped nanocomposites. In the presence of multidrug and multimetal resistant strains of *E. coli*, the breakthrough time decreases significantly. Zn-only doped nanocomposites are not photocatalytically active. In the absence of light, the nanocomposites are still effective in decontaminating water, although less efficient than under solar light irradiation. Electrostatic interaction, metal toxicity, and release of singlet oxygen (only in the Cu-doped and Cu/Zn-doped nanocomposites) are the three disinfection mechanisms by which these nanocomposites disinfect water. A regrowth study indicates the absence of any living *E. coli* cells in treated water even after 4 days. These data and the long hydraulic times (under gravity) exhibited by these nanocomposites during photodisinfection of water indicate an unusually high potential of these nanocomposites as efficient, affordable, and sustainable point-of-use systems for the disinfection of water in developing countries.

KEYWORDS: *disinfection, nanocomposite material, multidrug-resistant Escherichia coli, water, reactive oxygen species*

■ INTRODUCTION

Globally, water-related diseases are major causes of morbidity and mortality. The accessibility to safe drinking water continues to diminish daily; this is largely due to the fact that the discharge of pollutants from humans, agricultural wastewater, or hospital and industrial effluents increases on a daily basis and contaminates all water bodies. For instance, nitrates, cadmium, lead, mercury, polyaromatic hydrocarbons (PAHs), phosphates, and fluoride are examples of chemical contaminants found in water. Biological contaminants include

Received: January 19, 2019
Accepted: June 17, 2019
Published: June 17, 2019

ACS Publications © 2019 American Chemical Society

DOI: 10.1021/acsami.9b01212

harmful microorganisms and their metabolic products; these are the primary causes of some infectious diseases leading to high morbidity and mortality rates in Sub-Sahara Africa (SSA).[2] Pathogens in water are not just a primary health concern in developing countries but also globally.[3] For example, the recent Joint Monitoring Programme (JMP) report of the World Health Organization (WHO) and United Nations Children's Fund (UNICEF) suggests that more than 844 million people (many of whom reside in SSA) are still without access to improved and safe sources of drinking water (**WHO & UNICEF, 2017**). According to WHO in February 2018, contaminated drinking water is estimated to cause 502 000 diarrheal deaths each year.

Recently, statistics from WaterAid Nigeria reported that 57 million people in the country do not have access to safe water, and two-thirds of the Nigerian population (about 130 million people) do not have access to safe drinking water, leading to the death of almost 60 000 children under the age of five from diarrhea (WHO, 2017). Also, almost 2 billion people drink water contaminated with faeces, thus putting them at risk of contracting diseases (Newsletter, WHO April, 2017).

Of even higher importance is the presence of multidrug and multimetal resistant (MD-MMR) pathogens in potable water. This has been recognized by the WHO as one of the top three threats to human health.[4] The discharge of antibiotics into the environment encourages bacteria therein to adapt to their toxicity.[5] Although antibiotics are useful to humans, their misuse and overuse increase the presence of MD-MMR bacteria in water bodies, ultimately creating health challenges for humans and animals. This resistance has been further aggravated by the variety of brands and large amounts of antibiotics administered in clinics and hospitals.[6]

Water disinfection is the last and most vital step in the water and wastewater treatment process. It includes the destruction or removal of microorganisms.[7] A number of disinfection methods have been deployed for the removal of bacteria from water including physicochemical processes such as adsorption and biological filtration,[8] chlorination and ozonation,[9,10] electromagnetic irradiation,[11] photocatalysis,[12] metal disinfection,[9] and solar disinfection.[13,14]

Photocatalysis is arguably the most favored technique in recent times especially with photocatalysts that release reactive oxygen species that are nonselective to any microorganism. Furthermore, the technique does not produce harmful disinfection byproducts (DBPs) and resistant bacteria unlike chlorination and ozonation processes,[15,16] and it is cheap when compared with membrane filtration technique.[17] Furthermore, with the use of visible-light photocatalysts, especially those that are efficient with solar irradiation, bacteria regrowth is unlikely.[18] Finally, it eliminates the need for a constant power supply for water treatment; this aspect is in fact crucial for application in the developing countries because electric power supply is a major issue in these countries.

Most photocatalysts developed recently have been made via the sol–gel technique and quite some use titania and graphene.[19] The cost of titania, graphene, and several other transition metal oxides often used in these (laboratory scale) materials is, however prohibitive for large scale applications in developing countries and alternatives to these quite expensive materials are therefore of highest interest. This includes both the raw materials as such but also the process of fabrication of the materials.

The current study introduces the third generation of hybrid clay (HYCA) nanocomposites for disinfection of water containing *Escherichia coli* (including water bearing MD-MMR *Escherichia coli* (*E. coli*)) under solar light irradiation. Unlike the first- and second-generation HYCA, which are mainly useful for heavy metal removal and water disinfection via electrostatic interaction, respectively,[20,21] these third-generation HYCA composites have been doped with Cu and Zn using a solvothermal process and show extended disinfection efficiencies due to a reduced band gap that improves their activity in the visible-light region. In addition, most reports on water photodisinfection have used batch methods for their disinfection experiments. These experiments, although useful, typically provide a qualitative picture of the efficacy of a photocatalytic material but are often unreliable for quantification or longer term exposure studies. In contrast, the current study reports the use of a fixed-bed setup using gravity-driven liquid flow for our photodisinfection process. This approach truly mimics the real mode of water treatment on a large and continuous scale.

As stated above, the use of visible-light irradiation rather than special UV lamps aims at eliminating the additional costs needed to purchase these specialized lamps in a light driven decontamination system. In short, the nanocomposite materials reported in this study are easy to produce in less developed regions of the world, sustainable and cheap, yet very efficient in water disinfection. No high pressure nor additional (expensive) and environmentally harmful organic template is necessary. These nanocomposites will find potential application in the development of efficient low-cost point-of-use water treatment systems that can be deployed to rural communities where power supply is limited.

2.0. MATERIALS AND METHODS

2.1. Reagents/Materials. Reagents were used as obtained without further purification unless stated otherwise. Kaolinite clay was purified according to Adebowale et al.[22] *Carica papaya* seeds were obtained from different markets within Ede, Osun State, Nigeria, crushed with a mortar and pestle and sun-dried. They were crushed and packed into an airtight container for further use. Pure culture of the test bacteria utilized in this study: *E. coli* (ATCC 25922) and MD-MMR *E. coli* strains EC4 and EC6, were obtained from the Nigerian Institute of Medical Research (NIMR) Laboratory, Yaba, Lagos State, Nigeria and Department of Microbiology, University of Ibadan, Nigeria, respectively. Eosin methylene blue (Ozoid) was used to identify *E. coli* cells.

Metal-doped hybrid clays were prepared by forming a slurry from different weights of purified clay, crushed *Carica papaya* seeds, and $ZnCl_2$/$CuCl_2$ in the ratio: 1:1:2 wt/wt for Zn-doped and Cu-doped hybrid clay nanocomposites and 1:1:1:2 wt/wt of purified clay, crushed *Carica papaya* seeds, $CuCl_2$, and $ZnCl_2$ for Cu/Zn-doped hybrid clay nanocomposite. To all slurries was added 0.1 M NaOH solution and the resulting mixtures were continuously stirred for 24 h, dried in an oven at 105 °C, and transferred to a furnace where they were calcined at 500 °C under N_2 for 2 h. The resulting dark products were allowed to cool to room temperature, washed with Millipore water until neutral pH, and oven-dried at 105 °C. They were packed into an airtight container for further use. Similar procedure was applied for the preparation of calcined crushed *carica papaya* seeds and Kaolinite clay except that they were not treated with NaOH and metal salts. These were used as control to investigate the active photocatalytic component of prepared nanocomposites.

2.2. Preparation of Bacterial Culture and Assessment of Antibiotic Resistance. *Escherichia coli* (ATCC 25922) was used as the model microorganism in this study. Multiple antibiotic and multimetal resistant (MD-MMR) *E. coli* strains (EC_4 and EC_6)

isolated from a river receiving runoff from an e-waste dumpsite in Alaba International Market, Lagos, Nigeria, were used in this study. EC_4 and EC_6 strains of *E. coli* showed resistance to gentamicin, kanamycin, ciprofloxacin, tetracycline, florfenicol, sulphamethoxazole/trimethoprim, cefpodoxime, ceftazidime, imipenem, meropenem, ertapenem, Cu (800 μg/mL), Pb (1000 μg/mL), and Zn (600 μg/mL). Experimental details describing how the EC_4 and EC_6 *E. coli* strains were ascertained to be multidrug and multimetal resistant are described in section 1.0 of the Supporting Information. Bacteria in this study were grown in nutrient broth at 37 °C to exponential growth phase and cell counts were made.

2.3. Characterization of Materials. The morphology of the Kaolinite clay was studied on a JEOL JSM 6510 Scanning electron microscopy (SEM) equipped with an EDX spectrometer of Oxford (INCAx-act SN detector), while the nanocomposite materials (Zn-, Cu-, and Cu/Zn-doped) and the bacteria-loaded materials were studied using a field-emission scanning electron microscopy (FESEM, Carl Zeiss, Germany) equipped with an Energy Dispersive X-ray (EDX) spectrometer of Oxford (INCAx-act SN detector, Aztec Analysis Software, England) for determination of the elemental composition. Dry samples were placed on aluminum stubs using carbon tape. Transmission electron microscopy (TEM) measurements were done on a JEOL TEM 1010 microscope at 200 kV. X-ray Powder diffraction data were collected on a PANalytical Empyrean powder X-ray diffractometer in a Bragg−Brentano geometry with a PIXcel1D detector with Cu K_α radiation (λ= 1.5419 Å) operating at 40 kV and 40 mA. Flame atomic absorption spectroscopy (FAAS) for the analysis of Zn^{2+}, Cu^{2+}, Na^+, and K^+ ions in water effluent was performed on a Perkin Elmer Analyst 800 high performance FAAS at absorbance wavelengths of 213.9, 324.8 and 589.6, and 766.5 nm respectively using air/acetylene gas. Limits of detection were at 0.001 mg/L for Zn^{2+}, 0.0025 mg/L for Cu^{2+}, 0.015 mg/L for Na^+, and 0.003 mg/L for K^+. Infrared spectra of the composite adsorbents were obtained using a PerkinElmer spectrum 100 Fourier transform infrared (FTIR) spectrophotometer with universal attenuated total reflectance (ATR) sampling accessory (PerkinElmer, Waltham, USA). Raman measurements were performed on the WITec Alpha 300 RAS microscope (WITec, Ulm, Germany).

UV-Diffuse Reflectance Spectroscopy (UV-DRS) measurements were done on a LAMBDA 1050 UV-Vis spectrophotometer (Perkin Elmer, Waltham, USA). The pH at the point of zero charge (pH_{pzc}) of the nanocomposites which is the pH at which the total charges on the surface of the material is zero, was determined by the salt addition method described by Dayanada et al.[23] The singlet oxygen generation by the nanocomposites prepared in this study was verified by using the 9,10-anthracenediyl-bis(methylene) dimalonic acid (ABMDMA) fluorescent probe method. ABMDMA is an anthracene derivative that upon excitation in the ultraviolet (370 nm) exhibits strong emission in the blue spectral region (~407 nm). In the presence of singlet oxygen, ABMDMA is oxidized into its corresponding endoperoxide (photobleached) and a decrease in the blue emission is observed (Figure S1). For these experiments, ABMDMA solution was added to a cuvette containing the nanocomposite under study. The resulting mixture was then exposed to the ambient light in the laboratory (fluorescent lamp spectra, Figure S2) for different time intervals while the corresponding emission at 407 nm (λ_{exc} = 370 nm) was monitored in a Jobyn Yvon Fluorolog spectrofluorimeter. Agilent Cary Eclipse Fluorescence Spectrophotometer was used for the analysis of raw and calcined Kaolinite.

2.4. Photodynamic Water Disinfection. A sample of sterile water was initially checked using a selective agar for *E. coli* to ensure the absence of bacteria in the water. Cultured bacteria strains were then added to sterile water to prepare the desired concentration of the bacteria suspension. Quantification of bacteria was carried out using the optical method with the use of a UV-Vis spectrophotometer at a wavelength of 600 nm to record the absorbance. Absorbance value was converted to concentration to obtain the amount of bacteria colony forming unit (cfu) per milliliter using the software in https://www.chem.agilent.com/store/biocalculators/calcODBacterial.jsp

The estimated values were equivalent to 2.32×10^7 cfu/mL for *E. coli*, 7.80×10^8 cfu/mL for EC_6 strain, 5.09×10^8 cfu/mL for EC_4, 3.28×10^7 cfu/mL for EC_6 + *E. coli*, and 3.2×10^7 cfu/mL for EC_4 + EC_6. The suspensions were allowed to flow through the nanocomposites in a fixed bed under visible light from fluorescent lamps in the laboratory (spectrum of visible light from fluorescent lamps is shown in Figure S2. Preliminary investigations (section 4.0 in the Supporting Information) suggested that all three prepared nanocomposites were active against *E. coli* with Zn-doped and Cu/Zn-doped hybrid clay nanocomposites completely inactivating the bacteria after 2 h and the Cu-doped nanocomposite inactivating it after 6 h. Thus, these samples were used for further studies. Details of this study are given in Table S1.

In the fixed bed mode, a fixed weight (2.0 g) of each of the nanocomposites that were initially sterilized by dispersing in 70% ethanol and dried to constant mass at 105 °C, were packed in a 400 mm × 10 mm transparent glass column. The transparent glass column used was initially dry-sterilized at 160 °C for 2 h and primed by running 400 mL of sterile water through the packed glass column containing the nanocomposite material. Thereafter, suspensions of the test bacteria (normal *E. coli*, EC_4, and EC_6) at known concentrations (in cfu/ml) in sterile distilled water were passed through the column at a flow rate of 8 mL/min under natural solar light conditions. Although all three prepared nanocomposites were used to disinfect *E. coli* ATCC 25922 (normal strain), Cu/Zn-doped nanocomposite was used to disinfect EC_4, EC_6, EC_4 + EC_6 and EC_6 + *E. coli* ATCC 25922 strains in water. For experiment in the dark, an identical protocol (except for the absence of light) was used. Samples collected were cultured with selective Eosin Methylene Blue agar.

2.5. Bacteria Regrowth Study. Bacteria regrowth study was carried out following a slightly modified protocol from an earlier study, section 2.4. Samples collected at various time intervals were divided into two portions and kept in sample bottles. While one portion was left in an incubator the other was left on the laboratory bench. Samples were collected after every 24 h and the presence of living *E. coli* cells were determined using Eosin Methylene Blue agar.

2.6. Nanocomposite Regeneration. Autoclave heating equipment was used to regenerate spent hybrid clay nanocomposites (bacteria-loaded materials) for its reuse over several cycles. The exhausted or used nanocomposite was wrapped in an aluminum foil and placed inside an autoclave for 15 min at 121 °C, after which the nanocomposite material was dried in an oven at 105 °C and stored for reuse.

3.0. RESULTS AND DISCUSSION

Figure 1A shows the ATR-FTIR spectra of Kaolinite clay, *Carica papaya* seed, Cu-doped and Cu/Zn-doped nanocomposites. As expected, the peaks around 3650 cm^{-1} in the kaolinite spectrum are due to − O−H stretching motion of

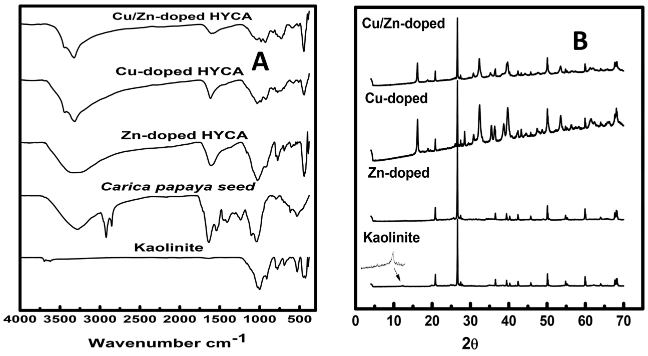

Figure 1. (A) ATR-FTIR spectra of kaolinite; *Carica papaya* seeds; and Zn-doped, Cu-doped, and Cu/Zn-doped hybrid clay nanocomposites. (B) X-ray-diffraction patterns for Kaolinite and Zn-doped, Cu-doped, and Cu/Zn-doped hybrid clay nanocomposites.

interlayer hydroxyl groups which are structurally important for Kaolinite because they keep the clay from swelling.[24,25] The small band appearing at 1628 cm^{-1} correspond to the − O−H bending vibration of water in the interlayer of the clay mineral. The Si−O stretching vibration is seen at 1001 cm^{-1}[26,27] while the shoulder at 910 cm^{-1} corresponds to Al−O bending vibrations. The peaks at 780 and 690 cm^{-1} show the existence of Al−OH bond vibrations.[20]

The *Carica papaya* seed spectrum shows a broad − O−H stretching vibration around 3283 cm^{-1}. Bands at 2925 and 2845 cm^{-1} represent the C−H stretching vibration of methyl and methylene groups, respectively. The strong peak at 1638 cm^{-1} may be due to a C═O stretching bond from amide groups.[28]

There is a new but weak band at 3444 cm^{-1} for Cu-doped and Cu/Zn-doped nanocomposites which is assigned to hydroxyl stretching from clinoatacamite[29] with its second intense peak at 3326 cm^{-1} from atacamite.[30] In contrast, the Zn-doped composite shows a broad band centered around 3324 cm^{-1} suggesting the presence of paratacamite.[31] The strong peak at 1608 cm^{-1} present in all three nanocomposite materials represents an overlap of −C═C− and −N−H in an aromatic ring,[32,33] which appears to be broader but less strong in the Cu/Zn-doped nanocomposite material.

Considering the fingerprint region (1000 to 500 cm^{-1}) for all three nanocomposite materials in comparison with raw kaolinite clay, the spectrum of the Zn-doped nanocomposite shows a pattern that is quite similar to that of kaolinite clay. However, Cu-doped and Cu/Zn-doped nanocomposites show different fingerprint signatures suggesting that new phases could have developed in these nanocomposites. The band at 451 cm^{-1} is typical of the presence of M-O bending vibrations in the nanocomposites due to the new mineral phase, paratacamite.[30] Furthermore, the peak at 582 cm^{-1} for Cu-doped and Cu/Zn-doped nanocomposites indicates the formation of Cu−O bonds.[34,35]

All three nanocomposites show an Al−O stretching vibration at 909 cm^{-1} while the peak at 3328 cm^{-1}, common to both Cu-doped and Cu/Zn-doped nanocomposites, indicates hydroxyl stretching frequency of atacamite mineral phase.[30] In the case of Zn-doped nanocomposite material, the 3328 cm^{-1} peak appears broad, perhaps due to H-bonding.

Raman spectra obtained at different locations of each sample show that the nanocomposites are heterogeneous (Figure S3). Considering the Zn-doped nanocomposite, bands at lower frequencies (200−350 cm^{-1}) are associated with Zn.[36] The peaks at 148 and 484 cm^{-1} are from structural lattice vibrations belonging to O−Al−O symmetric bend and Si−O−Si bending of quartz in Kaolinite clay (Figure S3I).[37] Broad bands around 2400 and 3300 cm^{-1} are present in the spectra of both kaolinite clay and crushed *Carica papaya* seeds. They represent −OH stretching vibrations[38] with the 2400 cm^{-1} band being more pronounced in the clay spectrum. In the spectra of the Cu-doped hybrid clay nanocomposite, the 282 and 630 cm^{-1} peaks are A_g and B_g Raman modes from tenorite CuO.[35] The band at 151 cm^{-1} corresponds to the O−Cu−O bending mode while the bands at 475 and 514 cm^{-1} belong to Cu−O and Cu−Cl of paratacamite and nantokite, respectively.[39] Raman analysis of the Cu/Zn-doped shows bands at 161, 463, and 3465 cm^{-1} which can be assigned to atacamite, Cu−Cl vibration of nantokite, and −OH bending of clinoatacamite, respectively.[39]

Powder X-ray diffraction (XRD) was used to analyze the phase and crystal structure of the materials. Figure 1B shows the XRD patterns of Kaolinite clay and the corresponding nanocomposites. The diffractograms of Kaolinite clay show a characteristic (001) reflection assigned to crystalline anorthic Kaolinite (001) at 2θ 12.4° (JCPDS 79−1570) with reflections assigned to quartz at 20.9, 26.7, 50.2, and at 60.0° (JCPDS 46−1045). The quartz reflections are common to all nanocomposites indicating that the quartz phase is unaltered by temperature during composite preparation.

However, the diffractograms of the Zn-doped nanocomposite show similar patterns to that of Kaolinite except for the absence of the (001) reflection peak of kaolinite. This peak was also absent in Cu-doped and Cu/Zn-doped hybrid clay nanocomposites (Figure 1B). However, the presence of new crystalline phases in the Cu-doped and Cu/Zn-doped nanocomposites is possibly linked to the higher melting point of the Cu^{2+} salt (498 °C), making $CuCl_2$ salt available for interaction with other components of the mixture during the synthesis of the composites at 500 °C. Nonetheless, with Cu-doped and Cu/Zn-doped hybrid clay nanocomposites, a new crystalline phase is seen at two positions in their diffractogram at 2θ 16.2 and 32.4° belonging to the (011) and (201) reflections respectively of the orthorhombic atacamite mineral with chemical formula of $Cu_2Cl(OH)_3$ (JCPDS 25−0269). In the case of the Cu-doped nanocomposite, this crystalline phase was identified as the monoclinic polymorph of atacamite called clinoatacamite ($Cu_2(OH)_3Cl$.[40] However, for Cu/Zn-doped nanocomposite, the rhombohedral atacamite mineral called the zincian paratacamite $[(Cu,Zn)_2(OH)_3Cl)]$ was identified by way of the reflections observed at 16.2, 30.7, 32.4, 39.7, 50.1, 53.5, 61.8, and 67.6° corresponding to the (200), (220), (400), (222), (333), (040), (426), and (532) reflections, respectively (JCPDS 25−0325). The XRD pattern of clinoatacamite and paratacamite minerals are similar but their unit cells differ.[40] The formation of clinoatacamite in water follows the reaction:[29]

$$2CuCl_2 + 3H_2O \leftrightarrow Cu_2(OH)_3Cl + 3HCl \quad (1)$$

Further investigation of the XRD diffractograms of both the Cu-doped and Cu/Zn-doped nanocomposites confirm the presence of yet another new crystalline phase in these nanocomposites. This new phase is tenorite (mainly CuO) and is more prominent (as inferred from the reflection intensities) in Cu-only doped sample than in the Cu/Zn-doped nanocomposites. The tenorite reflections are observed at 35.5, 38.7, and 66.2° 2θ in both Cu-doped and Cu/Zn-doped hybrid clay nanocomposites whereas other tenorite peaks were found at 61.4, and 65.9° (JCPDS 048−1548). Tenorite-like atacamite has a monoclinic crystal structure.[41] The tenorite phase found in both Cu nanocomposites probably is a result of the reaction between NaOH and $CuCl_2$ in the reacting system[34] which is presented in eq 2:[29]

$$CuCl_2 + 2NaOH \rightarrow Cu(OH)_2 + 2NaCl \quad (2)$$

The heating of the copper hydroxide produces CuO (tenorite) as shown in eq 3.

$$Cu(OH)_2 \rightarrow CuO(s) + H_2O \quad (3)$$

Although the X-ray diffractogram of Cu-doped and Cu/Zn-doped nanocomposites show similarities (albeit with different reflection intensities) the reflection at 2θ 28.4° in the pattern of the Cu-doped nanocomposite suggests the presence of an additional crystalline phase called nantokite which is CuCl.[42] This is supported with additional peaks at 47.5° and 56.1°. This indicates that the Cu(II) species in the initial $CuCl_2$ is reduced to Cu(I) in the course of the reaction. Presumably, this process involves the carbothermal reduction via the organic parts of the *carica papaya* seeds.

In general, the XRD analysis indicate a mixed phase of the clinoatacmite, tenorite and zincian paratacamite in Cu-doped and Cu/Zn-doped nanocomposites.

The morphologies and dimensions of the nanocomposites were examined using scanning electron microscopy (SEM, Figure 2). Field Emission SEM images of the kaolinite clay and its calcined form show similar particle morphology (Figure 2A, F). Cu-doped nanocomposite material (Figure 2B) contains roughly spherical particles which are mostly aggregated.[41] This is consistent with the presence of tenorite in the nanocomposite material which is in agreement with the X-ray diffractograms, (Figure 1B). The Zn-doped HYCA nanocomposite particles are also agglomerated (Figure 2C). Images obtained from the Cu/Zn-doped nanocomposites (Figure 2D) depict particles with rhombohedral morphology indicative of zincian paratacamite.[43,44] The densely packed nature of the nanocomposites is presumably, a consequence of the high temperatures used during sample preparation.[45]

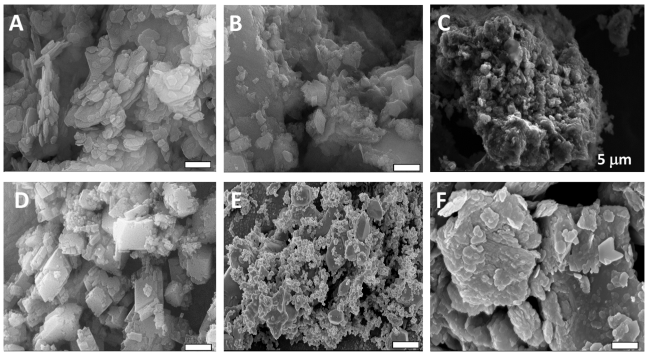

Figure 2. Field-emission scanning electron microscopy images of (A) kaolinite (B) Cu-doped (C) Zn-doped (D) Cu/Zn-doped Hybrid Clay (HYCA) nanocomposites (E) Calcined *Carica papaya* seeds (F) Calcined Kaolinite clay. All scale bar = 200 nm

The high-resolution transmission electron microscopy (HR-TEM) images of raw kaolinite and Cu/Zn-doped nanocomposite showed a change in the particle morphology with the nanocomposite having smaller-sized particles compared to the typical platelike structures observed for kaolinite clay particles (Figure S4).

The X-ray microanalysis data obtained from the composite materials are represented in Table S2. Table S2 shows that that the O, Al, and Si contents in the nanocomposite materials are significantly reduced compared to the starting material (kaolinite). The cause of this reduction is likely to be due to the presence of NaOH in the mixture during preparation of the composites that is known to leach Al and Si from clays.[46] The presence of the metals (Zn and Cu) in the nanocomposites suggest that their incorporation into the nanocomposites was successful.

The thermogravimetric (TG) and differential thermal analysis (DTA) curves, which characterize the thermal decomposition of the three nanocomposites, are shown in Figure 3. The Zn-doped nanocomposite shows a four-step weight loss. The first step from room temperature to 105.0 °C with a weight loss of about 20% is due to loss of water. A weight loss of 6.7% from 105.0 to 310.0 °C is due to the loss of structural water in the nanocomposites.[47] The third step of weight loss of 19.8% at 302−550 °C is the result of the degradation and volatization of the organic component of the nanocomposite. The corresponding DTA peaks at 79.0 and 431.0 °C indicate endothermic (desorption of water) and exothermic (degradation and volatization of organic content) processes, respectively. The absence of the typical kaolinite exothermic peak between 30.0 and 150.0 °C[20] supports our earlier X-ray diffraction claim of the destruction of the kaolinite structure.

The Cu-doped nanocomposite shows a three-step weight loss (Figure 3). A 3% weight loss between 25.0−166.0 °C is likely due to loss of adsorbed water, 11.8% at 117.0−328.0 °C due to phase transformation in the mixture (vaporization and sublimation possibly from the formation of the tenorite and clinoatacamite) and 11.3% at 329.0−656.0 °C owing to material decomposition. These assignments are qualitatively supported by the endothermic peaks in the DTA data (Figure 3) observed at 103.6, 265.4, and 458.0 °C, respectively. The phase transformation at 265.4 °C is suggested to be the dehydroxylation of atacamite while the double DTA exothermic peaks at 294.0 and 321.0 °C represent the stepwise loss of chlorine from the atacamite phase.[48−50] The phase

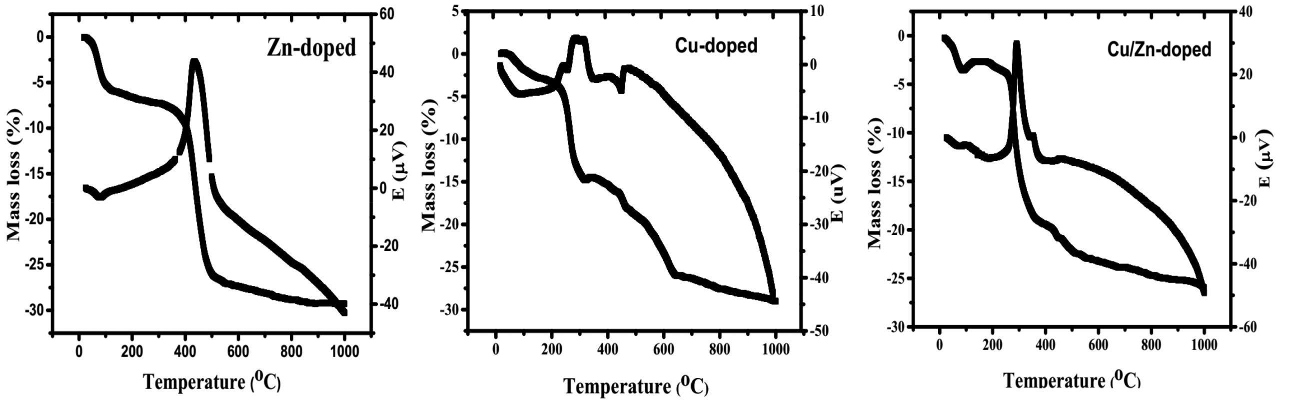

Figure 3. Thermal gravimetric (TG) and differential thermal analysis (DTA) plots for Zn-doped, Cu-doped, and Cu/Zn-doped hybrid clay nanocomposites.

DOI: 10.1021/acsami.9b01212
ACS Appl. Mater. Interfaces 2019, 11, 25483−25494

represented by the DTA peak at 458.0 °C can be assigned to the melting of CuCl (formed in the system during synthesis).

For the Cu/Zn-doped nanocomposite, the weight loss occurs in three main steps: 3.0% between 25.0 and 103.0 °C indicating loss of adsorbed water, 1.58% from 104.0 to 241.0 °C indicating the decomposition of organic components, and 16.0% from 242.0 to 394.0 °C representing phase transformation in the mixture that involves breaking of atomic bonds. The corresponding DTA analyses shows two endothermic peaks: 82.4 °C assigned to the release of adsorbed water and 457.0 °C assigned to the melting of CuCl (nantokite phase) in the nanocomposite.

The two exothermic peaks at 290.6 and 353.0 °C represent the stepwise loss of chlorine from the zincian paratacamite phase in the nanocomposite.[51] Overall, the nanocomposite samples are fairly stable, losing only ca. 30% of their weights up to 1000.0 °C. The results show that the materials are true composites and the doping of transition metals (Cu and Zn) into these nanocomposites was successful.

Water Disinfection Activity. The efficiency of the synthesized nanocomposites, Zn-doped, Cu-doped and Cu/Zn-doped hybrid clay, for the removal of the test organisms (*E. coli* ATCC 25922) in aqueous solution was evaluated using the fixed-bed mode at a flow rate of 8 mL/min. The results are presented in terms of the breakthrough times for the different composite adsorbents and are shown in Figure S5 (Supporting document).

The breakthrough time is defined here as the time for the first colony of bacteria to be identified in the effluent (treated water) from the column. The breakthrough times for these nanocomposites when water contaminated with 2.32×10^7 cfu/mL *E. coli* ATCC 25922 was passed through them were 1500 min (25 h) for Zn-doped hybrid clay, 1800 min (30 h) for Cu-doped hybrid clay, and 2100 min (35 h) for Cu/Zn-doped hybrid clay nanocomposites (Figure S5A−C). Zn-doped hybrid clay nanocomposite exhibits the lowest efficiency for the removal of this bacterial strain while Cu/Zn-doped hybrid clay nanocomposite presents the highest efficiency. The volume of *E. coli*-contaminated water treated by 2 g of each nanocomposite at a flow rate of 8 mL/min are 16.8 L for Cu/Zn-doped, 14.4 L for Cu-doped, and 12 L for Zn-doped hybrid clay nanocomposites. When multidrug- and metal-resistant strains of *E. coli* (EC_6 and EC_4) were used for the experiment, the breakthrough times for the most efficient nanocomposite (Cu/Zn-doped hybrid clay) reduced to 900 min (15 h) even when both MD-MMR *E. coli* strains (EC_6 + EC_4) were introduced into solution at the same time and when EC_6 strain was mixed with normal *E. coli* ATCC 25922 strain (Figure S5D−G). This is more than 50% reduction in breakthrough time when compared with the disinfection for *E. coli* ATCC 25922. The reason for this could be because of the 10-fold increase in bacteria load (in the case of EC_6 and EC_4) and the possible sharing of metal resistance mechanisms via horizontal gene transfer with members of the ATCC 25922 population in the mixed suspension[52] (in the case of EC6 + *E. coli* ATCC 25922). The high resistance of these MD-MMR *E. coli* strains to Cu and Zn (two of the metals used in the synthesis of the nanocomposites in this study) could also have contributed to this decrease in disinfection efficiency.

With experiments conducted in the dark using Cu-doped and Cu/Zn-doped hybrid clay nanocomposites with water containing *E. coli* ATCC 25922, there was a reduced efficiency. Cu-doped nanocomposite had a breakthrough time of 1320 min (22 h) and Cu/Zn-doped, 1440 min (24 h) (Figure S6). This is in contrast with 1800 min (30 h) and 2100 min (35 h) for the nanocomposites respectively, under visible-light exposure. These results suggests that these materials are still quite active as disinfecting agents in the dark although less efficient than in visible-light. While it is expected that photocatalysis is absent in the dark systems, the disinfection efficiencies of the nanocomposites in the dark may be linked to the release of toxic metals (Cu and Zn) that inactivates bacteria cells when absorbed by their cell walls. This is in addition to electrostatic interaction between the Zn-doped nanocomposite and the bacteria cell wall as will be discussed in the next section.

Mechanisms of Water Disinfection. *Electrostatic Interaction Mechanism.* To consider the mechanism of disinfection of these nanocomposites, we hypothesize that the surfaces of these nanocomposites were positively charged because test bacteria used in this study are Gram-negative bacteria that are known to be negatively charged above a pH of between 2.0 and 3.0.[53] This leads to electrostatic attraction between the nanocomposite surfaces and the negative surfaces of the *E. coli* bacteria which are known to contain PO_4^{3-} and COO^- functional groups on their cell wall.[6] This was predicted in our study using the pH_{pzc} which is the pH at which the sum of all the charges on the surface of the nanocomposite will be zero.[53] Consequently, the net surface charge of our prepared nanocomposites will become more positive as the pH of solution decreases below their pH_{pzc} and vice versa.[54] This holds true for Zn-doped and Cu/Zn-doped nanocomposites given that their pH_{pzc} values (7.3 and 7.8 respectively as shown in Figure 4) are above that of the measured bacteria aqueous medium (6.9) and are thus expected to have positive charges on their surfaces during the course of disinfection.

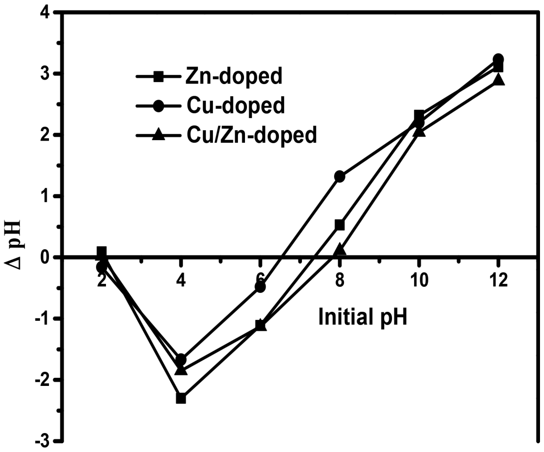

Figure 4. pH of point zero charge (pH_{pzc}) curves for synthesized Zn-, Cu-, and Cu/Zn-doped hybrid clay nanocomposites.

These positive charges on the surfaces of the nanocomposites are partly as a result of the presence of aluminol (Al−OH) on its surface which is known to have strong interaction with the carboxyl groups on the cell wall of the bacteria leading to bacterial adhesion on the nanocomposite.[55,56] However, the pH_{pzc} of Cu-doped nanocomposites is 6.5 and as such we do not expect an electrostatic attraction between the bacteria and the surface of this nanocomposite since its surface is expected to be negatively charged like that of the bacteria.

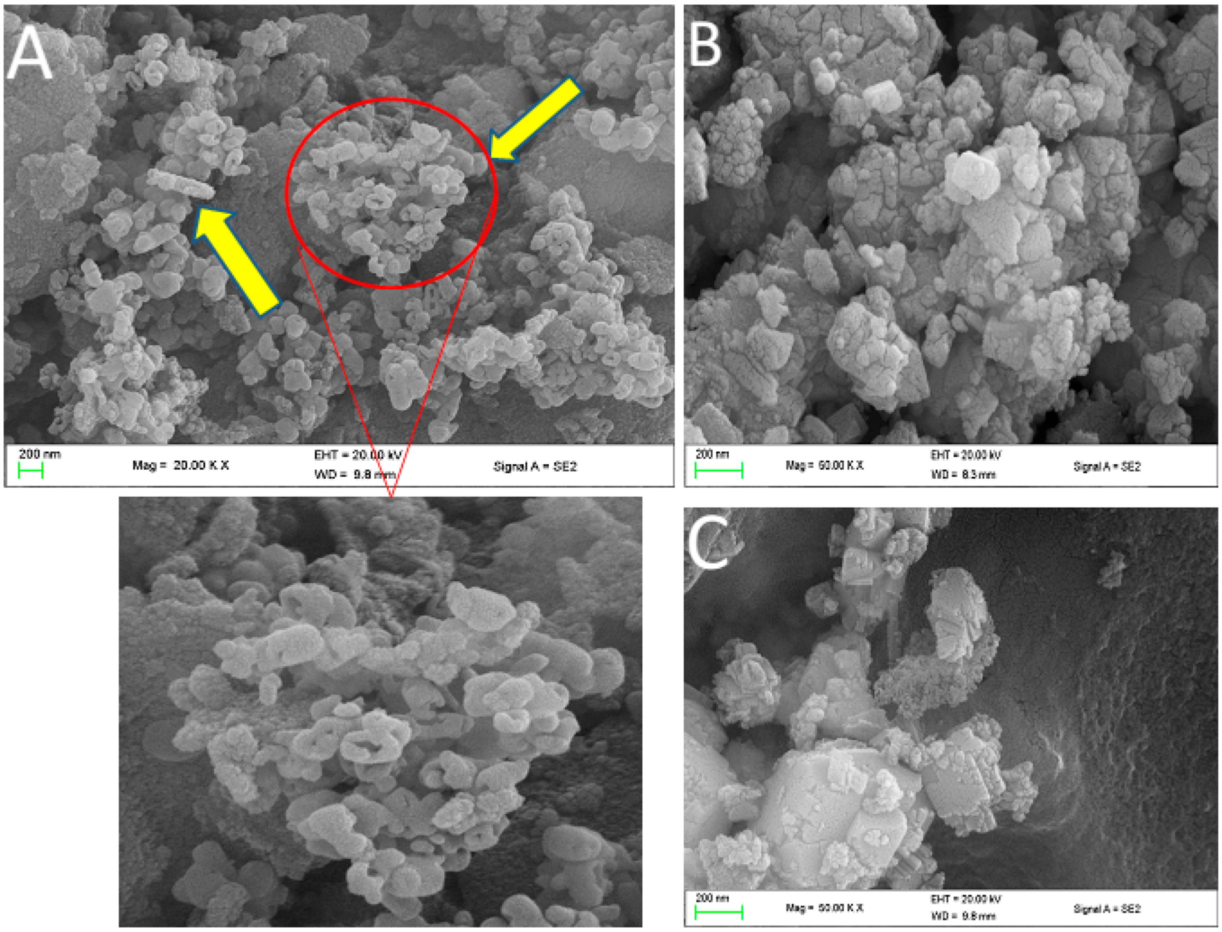

Figure 5. Field-emission scanning electron microscopy (FE-SEM) images of *E. coli*-loaded (A) Zn-doped, (B) Cu-doped, and (C) Cu/Zn-doped hybrid clay nanocomposites showing bacteria in lumps on the surface of the nanocomposite materials.

However, a close examination of FE-SEM images of bacteria-loaded particles of the nanocomposites (Figure 5A–C) reveals the presence of inactivated rod-like, curled and aggregated *E. coli* cells on the surface of Zn-doped hybrid clay nanocomposite while Cu-doped and Cu/Zn-doped nanocomposites did not show any bacteria on their surfaces. This indicates that our hypothesis of electrostatic interaction between bacteria and the surfaces of the nanocomposites for effective disinfection of water holds true only for Zn-doped nanocomposite. Cu-doped and Cu/Zn-doped nanocomposites are expected to inactivate bacteria by some other means as discussed in the next section.

Metal Toxicity Mechanism. All three nanocomposites do appear to disinfect *E. coli*-polluted water via metal toxicity due to leaching of Zn and Cu into treated effluent. It has been suggested that the release of metal ions into the local environment of the bacteria is effective in providing optimal antimicrobial activity via uptake of these metal ions by the bacteria.[57] To ascertain the leaching of metal ions during the disinfection process, treated water samples were analyzed for Cu and Zn using atomic absorption spectroscopy (AAS). The analysis suggested that there is a decrease in the metal found in solution with time of water disinfection (Figure 6A, B). However, with the Cu/Zn-doped nanocomposite, Cu tends to suppress the uptake of Zn by the bacteria after the first 3 h of the disinfection process (Figure 6C). Although Hassan et al.[58] recently observed a similar effect from Zn on the absorption of Cu by *Acenotobacter baumannii* strain ATCC 17978, there is need for more scientific evidence to prove this effect.

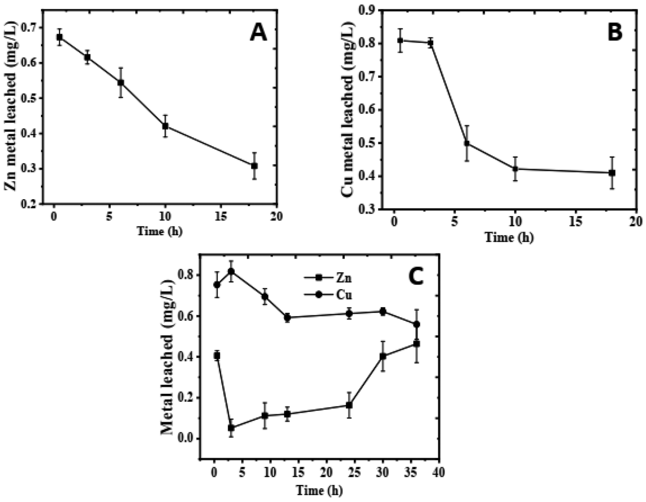

Figure 6. Metal leakage from (A) Zn-doped, (B) Cu-doped and (C) Cu/Zn-doped hybrid clay nanocomposites during the water disinfection process.

However, judging from the average water consumption per day for a healthy individual (3.5 L), the average amounts of Zn (0.51 mg/L) and Cu (0.8 mg/L) in the treated water are still well within the WHO 2017/2018 guidelines for drinking-water

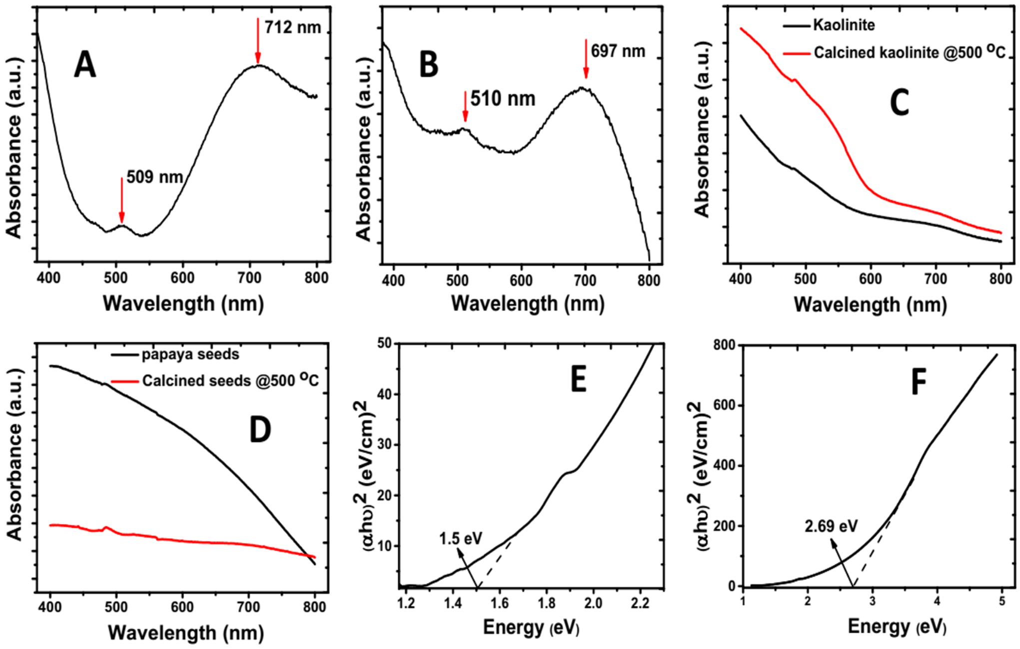

Figure 7. UV−vis diffuse reflectance spectra of (A) Cu/Zn-doped, (B) Cu-doped nanocomposites, (C) kolinite and calcined kaolinite, (D) *Carica papaya* seeds and calcined *Carica papaya* seeds; Tauc plots for band gap energy calculation of (E) Cu/Zn-doped and (F) Cu-doped nanocomposites.

quality, which accepts daily intake for adult humans as 15−22 mg/day for Zn and 2.0−3.0 mg/day for Cu. For children, the limits are 1.3 mg/day for Cu and 5−10 mg/day for Zn. These figures indicate that the treated drinking water are safe for both children and adults.

Photocatalysis Mechanism. To determine if there is a contribution from photocatalysis to the water disinfection from the nanocomposites, they were analyzed for their photocatalytic ability. UV−vis diffuse reflectance spectra (UV−vis DRS) show that both Cu-doped and Cu/Zn-doped nanocomposites absorb light in the visible region of the electromagnetic spectrum, depicting strong absorption peaks at approximately 511 and 700 nm (Figure 7A, B). The lowering of intensity of the absorption peak at ca. 510 nm (Figure 7A) arises from the presence of Zn^{2+} in the composite. However, the Zn-doped nanocomposite was not photoactive in the visible region (result not shown). We further investigated the component of the nanocomposite responsible for the photoactive nature of the material. While *carica papaya* seeds calcined under same conditions as the nanocomposites shows no evidence of absorption, the calcined kaolinite clay shows a weak absorption in the visible light region (Figure 7C, D).[1]

The band gap calculated using the Tauc plot methodology shows that the Cu/Zn-doped nanocomposite has a bandgap of 1.5 eV, while the Cu-doped materials have a band gap around 2.69 eV (Figure 7E−F). This suggests that the bandgap of kaolinite has been reduced from its typical energy of between 4.9 and 8.2 eV[1]. This effect (reduced bandgap) is due to the contribution from new secondary mineral phases of Zn and Cu as previously discussed.[59] Tenorite, for example, is one of the major new phases in both Cu-doped and Cu/Zn-doped nanocomposites prepared in this study. It absorbs light in the visible region with band gap of 1.2−1.8 eV.[60] Furthermore, Copper is known not only to extend optical absorption toward longer wavelengths but also to reduce charge recombination.[61−63] One other factor contributing to the narrowing of the band gap is the presence of carbon which is also a component of the nanocomposites in this study. It is one nonmetal known to induce the formation of intermediate energy levels in photocatalysts, enabling them to absorb visible-light.[64,65] Importantly, there is the d−d transitions in the Cu/Zn-doped nanocomposite, which further narrows the band gap[66] in the nanocomposite.

Reactive oxygen species (ROS) are usually released by photoactive materials for the degradation of organic molecules or microorganisms. One significant ROS, Singlet oxygen ($^1O_2$) is known to induce oxidation of lipids and proteins around cell membrane leading to cell death. It has been shown that $^1O_2$ does photomineralize bacteria, which explains our earlier observation that bacteria cells were not found on the surfaces of Cu-doped and Cu/Zn-doped nancomposites.[67,68] To verify the release of singlet oxygen from Cu/Zn-doped and Cu-doped nanocomposites exposed to ambient (white) light in the laboratory, similar to that of the sun, ABMDMA fluorescence intensity decay (taken at 407 nm) was measured as a function of the exposure time of the nanocomposites to laboratory illumination. The intensity decay plots are shown in Figure 8A and the corresponding emission spectra are presented in Figure S7.

The release of singlet oxygen upon exposure of the nanocomposites (in solution) to laboratory illumination provides further evidence for the long disinfection times (up to 36 h) experienced with these nanocomposites.

Photoluminescence (PL) analysis shown in Figure 8B supports our earlier claim from UV−Vis DRS analysis (spectra converted into absorbance in Figure 7) that both Cu/Zn-doped and Cu-doped nanocomposites are visible-light-active photocatalysts. When these nanocomposites are excited at 710 and 697 nm, they produced emissions in the near-infrared (NIR) region although with very low intensities (Figure 8C, D). Li et al.[69] have reported effective photocatalytic degradation of organic molecules in aqueous medium at NIR

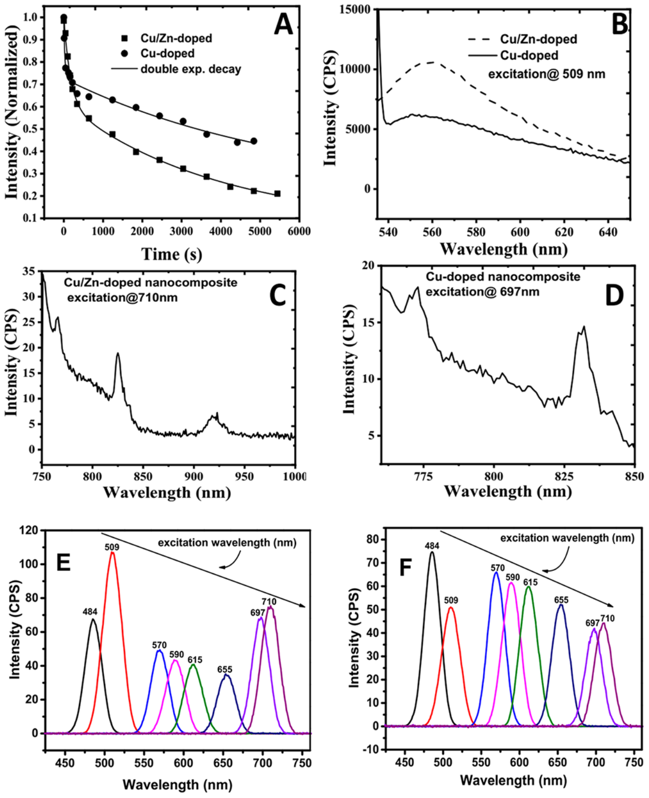

Figure 8. (A) Fluorescence Decay of ABMDMA @ 407 nm by (B) Photoluminescence spectra @ 509 nm excitation of Cu/Zn-doped and Cu-doped hybrid clay nanocomposites. Photoluminescence spectra of (C) Cu/Zn-doped nanocomposite @710 nm, (D) Cu-doped nanocomposite @ 697 nm, (E) Kaolinite clay, and (F) calcined kaolinite clay.

regions using a multifunctional single-phase photocatalyst doped with cobalt. It was suggested that doping with cobalt could have extended the response of the photocatalyst to light spectrum in the NIR region. In this study, doping the nanocomposites with Zn and Cu did follow similar behavior. This is an advantageous characteristic when coming to future experiments upon solar exposure because the sun spectrum also has a significant portion in the infrared. However, the PL analysis of both calcined kaolinite and *Carica papaya* seeds (Figure 8E, F) showed that both components did not contribute to the photoactive nature of the nanocomposites prepared in this study. They merely acted as substrates for the development of the nanocomposites.

To further prove the bacteria annihilation potential of metal-doped nanocomposites via photocatalysis and metal toxicity, treated effluent water samples were analyzed for the presence of K^+. The leakage of K^+ is an evidence of cell lysis that results from metal toxicity and/or interaction with singlet oxygen. It is known that K^+ participates in regulating the polysome content and protein synthesis of the bacterial cell.[70] Results from K^+ studies (Figure 9) indicate an increase in concentration of K^+ in the treated effluent water with treatment time of up to 1080 min (18 h).

In this study, it is obvious that *E. coli* cell lysis occurred via an interaction between bacterial cell and/or metals and singlet oxygen via visible-light irradiation on Cu-doped and Cu/Zn-doped hybrid clay nanocomposites. Zinc appears to be more toxic to bacteria cells when compared with Cu which may explain the higher K^+ values observed for Zn-doped treated effluent (Figure 9). Furthermore, there is the possibility of the presence of Cu to suppress Zn toxicity as seen from Cu/Zn-doped nanocomposites results in Figure 9.

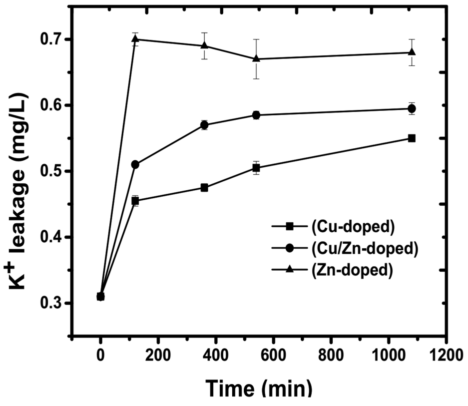

Figure 9. Potassium ion leakage of *E. coli* cells exposed to Zn-doped, Cu-doped, and Cu/Zn-doped hybrid clay nanocomposites (initial concentration of *E. coli* = 2.32 × 10^7 cfu/mL, temperature = 30 ± 2 °C; pH 6.9. Error bars indicate standard deviation of replicates (n = 2).

It is possible for adsorption and metal toxicity to occur at the same time. It is however not clear if all three proposed mechanisms: photocatalysis, electrostatic attraction and metal leaching occur simultaneously or if they happen serially in the course of disinfecting water using the nanocomposites reported in this study. However, given the results obtained from this study for disinfection of MD-MMR *E. coli* (with decrease in breakthrough time), we can safely conclude that the metal toxicity indeed played a significant role in disinfection but not as the sole disinfecting mechanism because the MD-MMR *E. coli* can tolerate higher concentrations of Cu and Zn in solutions than what was observed in this study.

Finally, result from regrowth experiments further supports our claim of bacteria cell death since there was no growth of *E. coli* (ATCC 25922) in treated water after 4 days for both Cu-doped and Cu/Zn-doped nanocomposites either through incubation or when left standing in sample vials under ambient laboratory conditions. This observation is complimented by the data from K^+ leakage test after the disinfection process. These all point to the fact that the treated water is safe for drinking even if left standing for 4 days at temperatures of up to 160 °C.

Regeneration Studies. It is not only important for a material to be efficient in the disinfection of water but it is also crucial from an economic perspective, to be able to reutilize the material over several cycles while retaining a good portion of its efficiency. The most efficient nanocomposite prepared in this study (Cu/Zn-doped hybrid nanocomposite) was subjected to investigations of its reusability. The Cu/Zn-doped nanocomposite was loaded with *E. coli* (2.32 × 10^7 cfu/mL) via column mode. At breakthrough point of 2160 min, the material was regenerated using the steam technique. Figure 10 shows the result from the two steam regeneration processes. With the steam regeneration method, it is observed that the disinfection efficiency of Cu/Zn-doped hybrid clay nanocomposite decreased upon regeneration with breakthrough times of 1800 min (volume of treated solution-14.4 L) and 1560 min (volume of treated solution-12.4 L) for the first and second regeneration cycles, respectively, compared with 2160

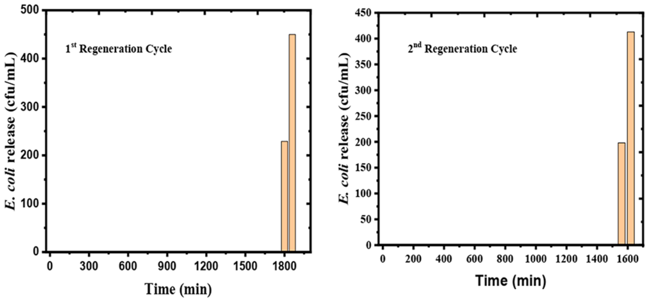

Figure 10. Breakthrough time plots for the regeneration of *E. coli*-loaded Cu/Zn-doped hybrid clay nanocomposite.

min (volume of treated solution-17.28 L) recorded before regeneration

CONCLUSION

This study provides extensive evidence of the potential of metal-doped hybrid clay materials for the disinfection of pathogens in water using *E. coli* as a model pathogen commonly encountered in drinking water. The results suggest that doping a mixture of kaolinite clay and *carica papaya* seeds with a combined dose of Zn and Cu produces a nanocomposite that has improved efficiency for water disinfection as compared to a mixture doped with single metal ions (Cu^{2+} or Zn^{2+}). This study shows that three mechanisms are responsible for the disinfecting properties of the metal-doped nanocomposites: electrostatic interaction, metal leaching, and photocatalysis via production of reactive singlet oxygen species that are capable of lysing bacteria cell wall, leading to cell death. It was verified that although the Zn-doped nanocomposite utilizes electrostatic interaction and metal leaching mechanisms, the Cu-doped nanocomposite operates through metal leaching and photocatalysis. The Cu/Zn-doped nanocomposite operates by all three mechanisms. When the most efficient nanocomposite (Cu/Zn-doped) was used to disinfect water loaded with the multidrug and multimetal resistant (MD-MMR) *E. coli* strains (EC_6 and EC_4) and a combination of the resistant and normal *E. coli* strains, its disinfection efficiency reduced by 50% due to the resistance shown by these MD-MMR *E. coli* strains to very high concentration of heavy metal ions. Results from regrowth experiments suggested that disinfection was complete and there were no possibilities of any inactivated bacteria cells regrowing in treated water. Regeneration studies of Cu/Zn-doped nanocomposite indicate a decrease in efficiency.

ASSOCIATED CONTENT

Ⓢ Supporting Information

The Supporting Information is available free of charge on the ACS Publications website at DOI: 10.1021/acsami.9b01212.

> Detailed description of isolation and antibiotic screening of multidrug and multimetal resistant *E. coli*, description of singlet oxygen determination, determination of solar spectra at ambient laboratory light, and description of disinfection process; figures for Raman spectroscopy analysis, table for EDX analysis of samples, figures of TEM images of samples, figures of breakthrough times of water disinfection, figure for dark experiment and fluorescence spectra of nanocomposite samples (PDF)

AUTHOR INFORMATION

Corresponding Author

* E-mail: unuabonahe@run.edu.ng. Tel: +2348053145971 (E.I.U.).

ORCID

Martins O. Omorogie: 0000-0001-9697-2960
Emmanuel I. Unuabonah: 0000-0001-9854-3924

Notes

The authors declare no competing financial interest.

ACKNOWLEDGMENTS

EIU and ASSC acknowledge the support from The Sao Paulo Research Foundation (FAPESP) through the grant project N. 2013/07793-6 (*CeRTEV – Center for Research, Technology and Education in Vitreous Materials*) and for the Visiting Professorship grant N. 2017/26803-3. EIU also acknowledge the Alexander von Humboldt Foundation, Germany, for a grant used to purchase Fluorescence Spectrophotometer used for part of this work. The authors acknowledge the support of Walter Faria and Raquel Vilela from the Laboratório de Espectroscopia de Materiais Funcionais (LEMAF), São Carlo Institute of Physics (IFSC), University of Sao Paulo, Sao Carlos, Brazil, who provided help with some analysis of samples.

REFERENCES

(1) Nisar, J.; Århammar, C.; Jämstorp, E.; Ahuja, R. Optical Gap and Native Point Defects in Kaolinite Studied by the GGA-PBE, HSE Functional, and GW Approaches. *Phys. Rev. B: Condens. Matter Mater. Phys.* **2011**, *84*, 075120.

(2) WHO, Two billion people drinking contaminated water. https://phys.org/news/2017-04-billion-people-contaminated.html . (Accessed November 14, 2018).

(3) Cotruvo, J. A.; Sobsey, M. D., Point-of-use water treatment for home and travel. In *Water and Health–Vol. II* [Online] Grabow, W., Ed.; EOLSS Publications: Paris, 2009; p 103.

(4) Bassetti, M.; Ginocchio, F.; Mikulska, M. New treatment options against gram-negative organisms. *Critical Care* **2011**, *15* (2), 215.

(5) Barancheshme, F.; Munir, M. Strategies to Combat Antibiotic Resistance in the Wastewater Treatment Plants. *Front. Microbiol.* **2018**, *8*, 2603.

(6) Tijani, J. O.; Fatoba, O. O.; Petrik, L. F. A Review of Pharmaceuticals and Endocrine-disrupting Compounds: Sources, Effects, Removal, and Detections. *Water, Air, Soil Pollut.* **2013**, *224*, 1770.

(7) Unuabonah, E. I.; Ugwuja, C. G.; Omorogie, M. O.; Adewuyi, A.; Oladoja, N. A. Clays for Efficient Disinfection of Bacteria in Water. *Appl. Clay Sci.* **2018**, *151*, 211–223.

(8) Kandasamy, J.; Vigneswaran, S.; Hoang, T.; Chaudhary, D. Waste Water Treatment Technologies: Adsorption and Biological Filtration in Wastewater Treatment. In *Encyclopedia of Life Support Systems*; EOLSS, 2009; p. 33.

(9) Roy, P. K.; Kumar, D.; Ghosh, M.; Majumder, A. Disinfection of Water by Various Techniques–Comparison Based on Experimental Investigations. *Desalin. Water Treat.* **2016**, *57*, 28141–28150.

(10) Von Gunten, U. Ozonation of Drinking Water: Oxidation Kinetics and Product Formation. *Water Res.* **2003**, *37*, 1443–1467.

(11) Ambashta, R. D.; Sillanpää, M. Water Purification Using Magnetic Assistance: A Review. *J. Hazard. Mater.* **2010**, *180*, 38–49.

(12) Yu, J. C.; Ho, W.; Yu, J.; Yip, H.; Wong, P. K.; Zhao, J. Efficient Visible-light-induced Photocatalytic Disinfection on Sulfur-doped Nanocrystalline Titania. *Environ. Sci. Technol.* **2005**, *39*, 1175–1179.

(13) Lonnen, J.; Kilvington, S.; Kehoe, S.; Al-Touati, F.; McGuigan, K. Solar and Photocatalytic Disinfection of Protozoan, Fungal and Bacterial Microbes in Drinking Water. *Water Res.* **2005**, *39*, 877–883.

(14) Blanco-Galvez, J.; Fernández-Ibáñez, P.; Malato-Rodríguez, S. Solar Photocatalytic Detoxification and Disinfection of Water: Recent Overview. *J. Sol. Energy Eng.* **2007**, *129*, 4−15.

(15) Roy, P. K.; Ghosh, M. Chlorine Resistant Bacteria Isolated from Drinking Water Treatment Plants in West Bengal. *Desalin. Water Treat.* **2017**, *79*, 103−107.

(16) Owoseni, M. C.; Olaniran, A. O.; Okoh, A. I. Chlorine Tolerance and Inactivation of Escherichia coli recovered from Wastewater Treatment Plants in the Eastern Cape, South Africa. *Appl. Sci.* **2017**, *7*, 810.

(17) Linden, K.; Murphy, J. R., Physical Agents. In *Global Water Pathogen Project* [Online] ;Rose, J. B., Jiménez-Cisneros, B., Eds.; UNESCO and Michigan State University, East Lansing, MI, 2017.

(18) Zhang, S.; Ye, C.; Lin, H.; Lv, L.; Yu, X. UV Disinfection Induces a VBNC State In *Escherichia Coli* And *Pseudomonas Aeruginosa*. *Environ. Sci. Technol.* **2015**, *49*, 1721−1728.

(19) Morales-Torres, S.; Pastrana-Martínez, L. M.; Figueiredo, J. L.; Faria, J. L.; Silva, A. M. Design Of Graphene-Based TiO$_2$ Photocatalysts—A Review. *Environ. Sci. Pollut. Res.* **2012**, *19*, 3676−3687.

(20) Unuabonah, E. I.; Günter, C.; Weber, J.; Lubahn, S.; Taubert, A. Hybrid Clay: A New Highly Efficient Adsorbent For Water Treatment. *ACS Sustainable Chem. Eng.* **2013**, *1*, 966−973.

(21) Unuabonah, E. I.; Kolawole, M. O.; Agunbiade, F. O.; Omorogie, M. O.; Koko, D. T.; Ugwuja, C. G.; Ugege, L. E.; Oyejide, N. E.; Günter, C.; Taubert, A. Novel Metal-Doped Bacteriostatic Hybrid Clay Composites For Point-Of-Use Disinfection Of Water. *J. Environ. Chem. Eng.* **2017**, *5*, 2128−2141.

(22) Adebowale, K.; Unuabonah, I.; Olu-Owolabi, B. Adsorption of some heavy metal ions on sulfate-and phosphate-modified kaolin. *Appl. Clay Sci.* **2005**, *29* (2), 145−148.

(23) Dayananda, D.; Sarva, V. R.; Prasad, S. V.; Arunachalam, J.; Parameswaran, P.; Ghosh, N. N. Synthesis Of Mgo Nanoparticle Loaded Mesoporous Al$_2$O$_3$ And Its Defluoridation Study. *Appl. Surf. Sci.* **2015**, *329*, 1−10.

(24) Tinti, A.; Tugnoli, V.; Bonora, S.; Francioso, O. Recent Applications Of Vibrational Mid-Infrared (IR) Spectroscopy For Studying Soil Components: A Review. *J. Central Eur. Agric.* **2015**, *16*, 1−22.

(25) Schuttlefield, J. D.; Cox, D.; Grassian, V. H. An Investigation Of Water Uptake On Clays Minerals Using ATR FTIR Spectroscopy Coupled With Quartz Crystal Microbalance Measurements. *J. Geophys. Res.: Atmos.* **2007**, *112*, 1−14.

(26) Müller, C. M.; Pejcic, B.; Esteban, L.; Delle Piane, C.; Raven, M.; Mizaikoff, B. Infrared Attenuated Total Reflectance Spectroscopy: An Innovative Strategy For Analyzing Mineral Components In Energy Relevant Systems. *Sci. Rep.* **2015**, *4*, 6764.

(27) Rytwo, G.; Zakai, R.; Wicklein, B. The Use Of ATR-FTIR Spectroscopy For Quantification Of Adsorbed Compounds. *J. Spectrosc.* **2015**, *2015*, 727595.

(28) Simonescu, C. M. Application of FTIR spectroscopy in environmental studies. In *Advanced Aspects of Spectroscopy*; InTech: 2012.

(29) Engelbrekt, C.; Malcho, P.; Andersen, J.; Zhang, L.; Ståhl, K.; Li, B.; Hu, J.; Zhang, J. Selective Synthesis Of Clinoatacamite Cu$_2$(OH)$_3$Cl And Tenorite Cuo Nanoparticles By pH Control. *J. Nanopart. Res.* **2014**, *16*, 2562.

(30) Frost, R. L.; Martens, W.; Kloprogge, J. T.; Williams, P. A. Raman Spectroscopy Of The Basic Copper Chloride Minerals Atacamite And Paratacamite: Implications For The Study Of Copper, Brass And Bronze Objects Of Archaeological Significance. *J. Raman Spectrosc.* **2002**, *33*, 801−806.

(31) Martens, W.; Frost, R. L.; Williams, P. A. Raman And Infrared Spectroscopic Study Of The Basic Copper Chloride Minerals - Implications For The Study Of The Copper And Brass Corrosion And “Bronze Disease. *Neues Jahrb. Mineral., Abh.* **2003**, *178*, 197−215.

(32) Chadefaux, C.; Le Hô, A.-S.; Bellot-Gurlet, L.; Reiche, I. Curve-Fitting Micro-ATR-FTIR Studies Of The Amide I And II Bands Of Type I Collagen In Archaeological Bone Materials. *e-Preserv. Sci.* **2009**, *6*, 129−137.

(33) Li, G.; Magana, D.; Dyer, R. B. Photoinduced Electron Transfer In Folic Acid Investigated By Ultrafast Infrared Spectroscopy. *J. Phys. Chem. B* **2012**, *116*, 3467−3475.

(34) Luna, I. Z.; Hilary, L. N.; Chowdhury, A. S.; Gafur, M.; Khan, N.; Khan, R. A. Preparation and Characterization of Copper Oxide Nanoparticles Synthesized via Chemical Precipitation Method. *Open Access Lib. J.* **2015**, *2*, 1−8.

(35) Debbichi, L.; Marco de Lucas, M.; Pierson, J.; Kruger, P. Vibrational Properties Of Cuo And Cu$_4$O$_3$ From First-Principles Calculations, And Raman And Infrared Spectroscopy. *J. Phys. Chem. C* **2012**, *116*, 10232−10237.

(36) Alsayoud, A. Q.; Venkateswara Rao, M.; Edwards, A. N.; Deymier, P. A.; Muralidharan, K.; Potter Jr, B.; Runge, K.; Lucas, P. Structure Of ZnCl$_2$ Melt. Part I: Raman Spectroscopy Analysis Driven By Ab Initio Methods. *J. Phys. Chem. B* **2016**, *120*, 4174−4181.

(37) Saikia, B. J.; Parthasarathy, G.; Borah, R.; Borthakur, R. Raman And FTIR Spectroscopic Evaluation Of Clay Minerals And Estimation Of Metal Contaminations In Natural Deposition Of Surface Sediments From Brahmaputra River. *International Journal of Geosciences* **2016**, *7*, 873−883.

(38) Johansson, U. Surface Reactions On Kaolinite Studied By FT-Spectroscopy. *LICENTIATE THESIS*; Luleå Tekniska Universitet, Luleå, Sweden, 1997.

(39) Frost, R. L. Raman Spectroscopy Of Selected Copper Minerals Of Significance In Corrosion. *Spectrochim. Acta, Part A* **2003**, *59*, 1195−1204.

(40) Braithwaite, R.; Mereiter, K.; Paar, W.; Clark, A. Cu$_3$Zn(OH)$_6$Cl$_2$, A New Species, And The Definition Of Paratacamite. *Mineral. Mag.* **2004**, *68*, 527−539.

(41) Ratnawulan; Fauzi, A. Effect of calcination temperature on phase transformation and crystallite size of copper oxide (CuO) powders. *AIP Conf. Proc.* **2017**, 060009.

(42) Li, C.-T.; Tarhay, L. Identification of CuCl in Si by XRD-XRF Analysis. *JCPDS-International Centre for Diffraction Data* **2000**, *43*, 366−375.

(43) Chu, S.; Müller, P.; Nocera, D. G.; Lee, Y. S. Hydrothermal Growth Of Single Crystals Of The Quantum Magnets: Clinoatacamite, Paratacamite, And Herbertsmithite. *Appl. Phys. Lett.* **2011**, *98*, 092508.

(44) Yang, H.; Barton, I. F.; Andrade, M. B.; Downs, R. T. Crystal Structure Of A New Compound, CuZnCl(OH)$_3$, Isostructural With Botallackite. *Am. Mineral.* **2016**, *101*, 986−990.

(45) Ashok, C.; Rao, K. V.; Chakra, C. S. Facile Synthesis and Characterization of ZnO/CuO Nanocomposite for Humidity Sensor Application. *J. Adv. Chem. Sci.* **2016**, *7*, 223−226.

(46) Langston, R.; Jenne, E. Naoh Dissolution Of Some Oxide Impurities From Kaolins. *Clays Clay Miner* **1963**, *12*, 633−647.

(47) Gulgun, Y. The Effects Of Temperature On The Characteristics Of Kaolinite And Bentonite. *Sci. Res. Essays* **2011**, *6*, 1928−1939.

(48) Garcia-Martinez, O.; Millan, P.; Rojas, R. (-Cu$_2$(OH)$_3$Cl As Precursor In The Preparation Of Copper (I) And (II) Oxides And Copper Powder. *J. Mater. Sci.* **1986**, *21*, 4411−4418.

(49) Sharkey, J.; Lewin, S. Thermochemical Properties Of The Copper (II) Hydroxychlorides. *Thermochim. Acta* **1972**, *3*, 189−201.

(50) Ramamurthy, P.; Secco, E. Studies On Metal Hydroxy Compounds. VII. Thermal Analyses Of Copper Derivatives. *Can. J. Chem.* **1969**, *47*, 2185−2190.

(51) Fleischer, M. New Mineral Names. *Am. Mineral.* **1973**, *58*, 347−349.

(52) Hemme, C. L.; Green, S. J.; Rishishwar, L.; Prakash, O.; Pettenato, A.; Chakraborty, R.; Deutschbauer, A. M.; Van Nostrand, J. D.; Wu, L.; He, Z.; et al. Lateral Gene Transfer In A Heavy Metal-Contaminated-Groundwater Microbial Community. *M Bio* **2016**, *7*, No. e02234-15.

(53) Kang, J.-K.; Lee, C.-G.; Park, J.-A.; Kim, S.-B.; Choi, N.-C.; Park, S.-J. Adhesion Of Bacteria To Pyrophyllite Clay In Aqueous Solution. *Environ. Technol.* **2013**, *34*, 703−710.

(54) Unuabonah, E. I.; Agunbiade, F. O.; Alfred, M. O.; Adewumi, T. A.; Okoli, C. P.; Omorogie, M. O.; Akanbi, M. O.; Ofomaja, A. E.; Taubert, A. Facile Synthesis Of New Amino-Functionalized Agrogenic Hybrid Composite Clay Adsorbents For Phosphate Capture And Recovery From Water. *J. Cleaner Prod.* **2017**, *164*, 652−663.

(55) Lukasik, J.; Cheng, Y.-F.; Lu, F.; Tamplin, M.; Farrah, S. R. Removal Of Microorganisms From Water By Columns Containing Sand Coated With Ferric And Aluminum Hydroxides. *Water Res.* **1999**, *33*, 769−777.

(56) Lee, C.-G.; Park, S.-J.; Han, Y.-U.; Park, J.-A.; Kim, S.-B. Bacterial Attachment And Detachment In Aluminum-Coated Quartz Sand In Response To Ionic Strength Change. *Water Environ. Res.* **2010**, *82*, 499−505.

(57) Ren, G.; Hu, D.; Cheng, E. W.; Vargas-Reus, M. A.; Reip, P.; Allaker, R. P. Characterisation Of Copper Oxide Nanoparticles For Antimicrobial Applications. *Int. J. Antimicrob. Agents* **2009**, *33*, 587−590.

(58) Hassan, K. A.; Pederick, V. G.; Elbourne, L. D.; Paulsen, I. T.; Paton, J. C.; McDevitt, C. A.; Eijkelkamp, B. A. Zinc Stress Induces Copper Depletion In *Acinetobacter Baumannii*. *BMC Microbiol.* **2017**, *17*, 59.

(59) Xie, W.; Li, R.; Xu, Q. Enhanced Photocatalytic Activity Of Se-Doped TiO_2 Under Visible Light Irradiation. *Sci. Rep.* **2018**, *8*, 1−10.

(60) Cardiel, A. C.; McDonald, K. J.; Choi, K.-S. Electrochemical Growth Of Copper Hydroxy Double Salt Films And Their Conversion To Nanostructured P-Type Cuo Photocathodes. *Langmuir* **2017**, *33*, 9262−9270.

(61) Di Paola, A.; Garcıa-López, E.; Ikeda, S.; Marcı, G.; Ohtani, B.; Palmisano, L. Photocatalytic Degradation Of Organic Compounds In Aqueous Systems By Transition Metal Doped Polycrystalline TiO_2. *Catal. Today* **2002**, *75*, 87−93.

(62) Wetchakun, N.; Wanwaen, P.; Phanichphant, S.; Wetchakun, K. Influence Of Cu Doping On The Visible-Light-Induced Photocatalytic Activity Of $InVO_4$. *RSC Adv.* **2017**, *7*, 13911−13918.

(63) Sun, H.; Yip, H. Y.; Jiang, Z.; Ye, L.; Lo, I. M. C.; Wong, P. K. Facile Synthesis Of Oxygen Defective BiO_2-X For Visible-Light Driven Photocatalytic Inactivation Of *Escherichia Coli*. *J. Mater. Chem. A* **2018**, *6*, 4997−5005.

(64) Lavand, A. B.; Malghe, Y. S. Synthesis, Characterization And Visible Light Photocatalytic Activity Of Nitrogen-Doped Zinc Oxide Nanospheres. *J. Asian Ceramic Soc.* **2015**, *3*, 305−310.

(65) Zhang, X.; Qin, J.; Hao, R.; Wang, L.; Shen, X.; Yu, R.; Limpanart, S.; Ma, M.; Liu, R. Carbon-Doped ZnO Nanostructures: Facile Synthesis And Visible Light Photocatalytic Applications. *J. Phys. Chem. C* **2015**, *119*, 20544−20554.

(66) Qamar, M. T.; Aslam, M.; Ismail, I. M.; Salah, N.; Hameed, A. Synthesis, Characterization, And Sunlight Mediated Photocatalytic Activity Of CuO Coated ZnO For The Removal Of Nitrophenols. *ACS Appl. Mater. Interfaces* **2015**, *7*, 8757−8769.

(67) Markowska-Szczupak, A.; Rokicka, P.; Wang, K.; Endo, M.; Morawski, A.; Kowalska, E. Photocatalytic Water Disinfection under Solar Irradiation by D-glucose-modified Titania. *Catalysts* **2018**, *8*, 316.

(68) Bodzek, M.; Rajca, M. Photocatalysis in the Treatment and Disinfection of Water. Part I. Theoretical backgrounds. *Ecol. Chem. Eng. S* **2012**, *19*, 489−512.

(69) Li, X.; Zhu, Z.; Li, F.; Huang, Y.; Hu, X.; Huang, H.; Peng, R.; Zhai, X.; Fu, Z.; Lu, Y. Multifunctional Single-Phase Photocatalysts: Extended Near Infrared Photoactivity And Reliable Magnetic Recyclabilityz. *Sci. Rep.* **2015**, *5*, 15511.

(70) Das, S.; Sinha, S.; Das, B.; Jayabalan, R.; Suar, M.; Mishra, A.; Tamhankar, A. J.; Lundborg, C. S.; Tripathy, S. K. Disinfection Of Multidrug Resistant *Escherichia Coli* By Solar-Photocatalysis Using Fe-Doped ZnO Nanoparticles. *Sci. Rep.* **2017**, *7*, 104.

Visible-Light Mediated Photodynamic Water Disinfection @ Bimetallic Doped Hybrid Clay Nanocomposites

Chidinma G. Ugwuja[1,2], Olawale O. Adelowo[3], Aemere Ogunlaja[1,4], Martins O. Omorogie[1,2], Olumide D. Olukanni[1,2], Odion O. Ikhimiukor[3], Ievgeniia Iermak[5], Gabriel A. Kolawole[1,2,6], Christina Guenter[7], Andreas Taubert[8], Olusola Bodede[9], Roshila Moodley[9], Natalia M. Inada[5], Andrea S.S. de Camargo[5], Emmanuel I. Unuabonah[1,2,5*]

[1]African Centre of Excellence for Water and Environmental Research (ACEWATER), Redeemer's University, PMB 230, Ede, Osun State, Nigeria

[2]Department of Chemical Sciences, Redeemer's University, PMB 230, Ede, Osun State, Nigeria

[3]Department of Microbiology, University of Ibadan, Ibadan

[4]Department of Biological Sciences, Redeemer's University, P.M.B 230, Ede, Osun State, Nigeria

[5]São Carlos Institute of Physics, University of São Paulo, Av. Trabalhador Sãocarlense 400, 13566-590, São Carlos, Brazil

[6]Department of Chemistry, University of Zululand, Kwadlangezwa, 3886, Republic of South Africa

[7]Institute of Geosciences, University of Potsdam, D-14476 Potsdam, Germany

[8]Institute of Chemistry, University of Potsdam, D-14476 Potsdam, Germany

[9]School of Chemistry and Physics, University of KwaZulu-Natal, Westville Campus, Durban, South Africa

Corresponding Author
E. I. Unuabonah
E-mail: unuabonahe@run.edu.ng
Tel: +2348053145971

1.0 Isolation, Heavy metal and Antibiotic Screening of Multi-drug and Multi-metal Resistant *E. coli* (EC_4 and EC_6)

The strains were obtained from water samples collected from a river near the e-waste dumpsite at the Alaba International market, Lagos, Nigeria. Aliquots (100µl) of serially diluted samples (10^{-2}) were spread on Eosin Methylene Blue (EMB) agar plates. Colonies appearing as green metallic sheen were sub-cultured and purified on fresh EMB agar plates to obtain presumptive *E. coli* isolates (EC_4 and EC_6) [1]. The identities of the presumptive *E. coli* isolates were confirmed by Enterobacterial Repetitive Intergenic Consensus- Polymerase Chain Reaction (ERIC-PCR). The isolates were further tested for tolerance to Cu, Pb and Zn used as $CuSO_4$, $Pb(CH_3COO)_2$ and $ZnSO_4$ respectively [2]. Overnight cultures of *E. coli* isolates were streaked on Mueller Hinton Agar (MHA) plates supplemented with increasing concentrations (50 -1100 µg/ml) of the metals. The plates were incubated at 37 °C for 24-72 h and cell growth observed. Further, antibiotic susceptibility of the strains was carried out using the disc diffusion method previously described [3]. Overnight cultures of the strains were standardized in normal saline (0.85%) to conform to 0.5 McFarland turbidity standard and spread on the surface of MHA using sterile swab sticks. Discs of antibiotic used include; gentamicin (10µg), kanamycin (30µg), cefpodoxime (30µg), ceftazidime (30µg), Ertapenem (10µg), Imipenem (10µg) meropenem (10µg), ciprofloxacin (5µg), sulphamethoxazole/trimethoprim (23.75/1.25), florfenicol (30µg) and tetracycline (30 µg) (Oxoid Ltd.). Discs were placed aseptically on MHA plates previously inoculated with saline suspensions of the test bacteria. The plates were incubated at 37 °C for 24 h after which zones of growth inhibition around each antibiotic disc was measured and interpreted using recommended breakpoints by the Clinical and Laboratory Standards Institute [3].

2.0 Determination of Singlet Oxygen

The generation of singlet oxygen by the nanocomposites prepared in this study was determined by using the 9, 10-anthracenediyl-bis(methylene) dimalonic acid (ABMDMA) fluorescent probe. ABMDMA is an anthracene derivative that is photo bleached by singlet oxygen to produce the corresponding endoperoxide ABMDMA (Fig. S1) via an oxidation process. The photobleaching reaction was measured by recording the decrease in absorbance emission intensity of ABMDMA at 407 nm.

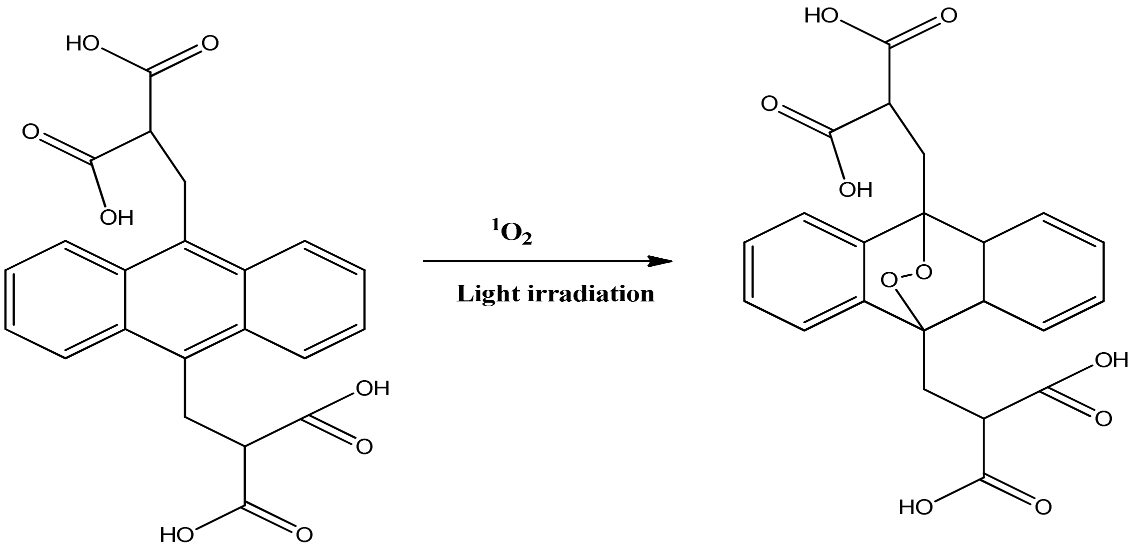

ABMDMA

Endoperoxide ABMDMA

Fig. S1: Reaction Scheme for 9, 10-anthracenediyl-bis(methylene) dimalonic acid and singlet oxygen generated from prepared nanocomposites.

For the experiment, 3 drops of 2 M of NaOH was added to 0.25 mg/mL of ABMDMA (in water). This stock solution was used fresh. A mixture of 1 mg/mL of the nanocomposite materials were prepared and prior to analysis, 30 μL of the ABMDMA stock solution was added to the mixture in the dark. The first measurement at 0 sec was measured preparing and keeping the fresh solution in the dark and then submitting it to excitation at 370 nm and fluorescence detection in the 390-

550 nm range, using a Fluorolog-3 HORIBA spectrophotometer (FluorEssenceTM software). This cycle was then repeated for the same sample, under same excitation and emission detection conditions, upon exposure of the solution to ambient light (fluorescent lamp in the lab) during different time intervals.

3.0 Determination of Solar Spectra at Ambient Light in Laboratory Used for Solar Disinfection-Singlet Oxygen Generation

In order to determine the spectra of light in the laboratory used for disinfection, the Ocean Optics USB2000+ Spectrometer was used under the following conditions:

Spectral Range: 180 to 880 nm

Integration Time: 1 ms to > 60 seconds

Optical Resolution: 0.3 to 10.0 nm FWHM (full-width half-maximum)

Operating Software: SpectraSuite

Fiber Optic Connector: SMA 905 to single-strand optical fiber (an optical fiber, we just let the light enter the spectrometer through the connector)

The plot of the spectra is show in Figure S2.

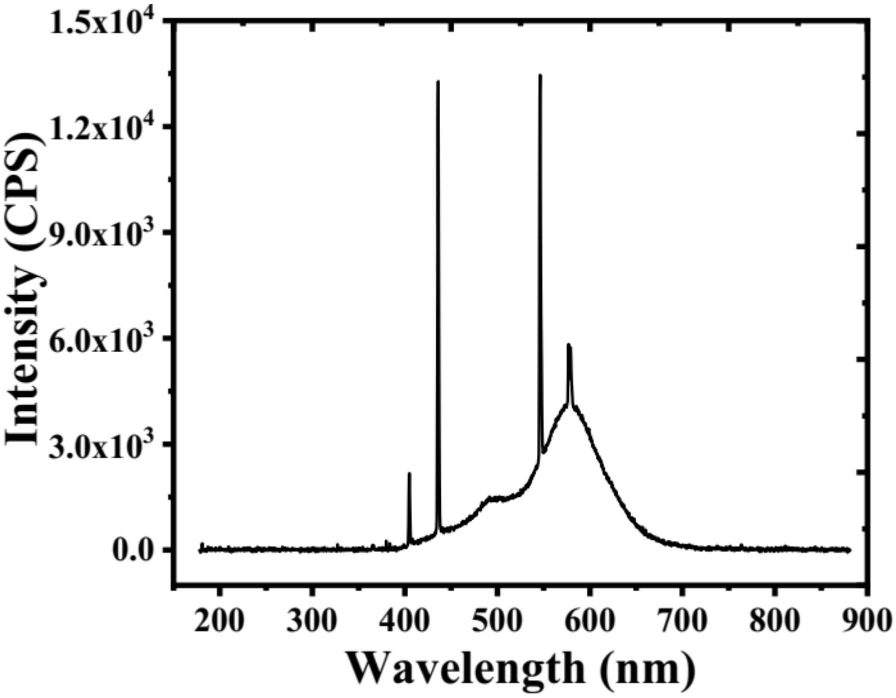

Fig. S2: Fluorescent Lamp Spectra Inside the Laboratory.

4.0 Preliminary Disinfection Investigation

To preliminarily ascertain the disinfection potentials of each of the prepared nanocomposite material, a batch experiment was carried out using *E. coli* ATCC 25922. The bacteria solution was diluted from the stock solution with saline water (0.9% NaCl solution) to the desired concentration of 2.32 x 10^7 cfu/mL for the experiment. The batch experiment carried out by adding 30 mg of each nanocomposite material to a sterilized conical flask containing 10 mL of the bacteria solution with the known concentration. Thereafter, all conical flasks were properly sealed and agitated at 150 rpm at 25 ^{o}C and exposed to natural ambient light in the laboratory (Fig. S2). Supernatants were collected at 2 h and 6 h and analyzed for bacterial concentration by measuring the optical density of the effluent using a UV-VIS spectrophotometer at 600 nm (OD600). Results shown in Table 1 suggest that all three prepared nanocomposites were active against *E. coli* with Zn-doped and Cu/Zn-doped hybrid clay nanocomposites completely inactivating the bacteria after 2 h and Cu-doped nanocomposite, after 6 h.

Table S1: Analysis of batch disinfection analysis of *E. coli* using Zn-doped, Cu-doped and Cu/Zn-doped hybrid clay nanocomposites.

Time (h)	Concentration (cfu/mL)		
	Zn-doped	Cu-doped	Cu/Zn-doped
0	2.32 x 10^7	2.32 x 10^7	2.32 x 10^7
2	0(100)*	1.76 x 10^7(24)*	0 (100)*
6	0 (100)*	0 (100)*	0 (100)*

Values in bracket = % removal

5.0 Raman Spectroscopy Analysis

Raman measurements were performed on the WITec Alpha 300 RAS microscope (WITec, Ulm, Germany). The excitation wavelength was 532 nm, detection range was 100-3600 cm^{-1}. The spectra were collected with 20x magnification objective (Zeiss, Jena, Germany). Spectra were recorded with integration time of 120 s and 2 accumulations for one spectrum. Obtained spectra were processed using WITec Project FOUR software and Origin 2016 software.

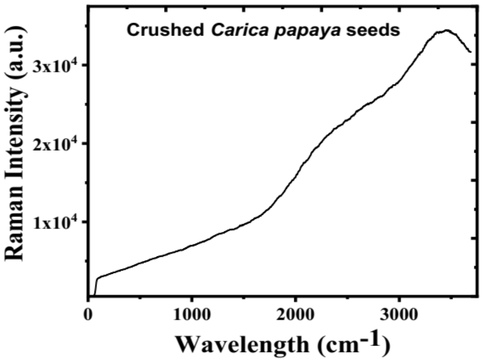

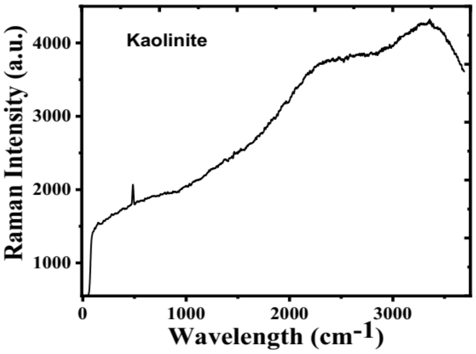

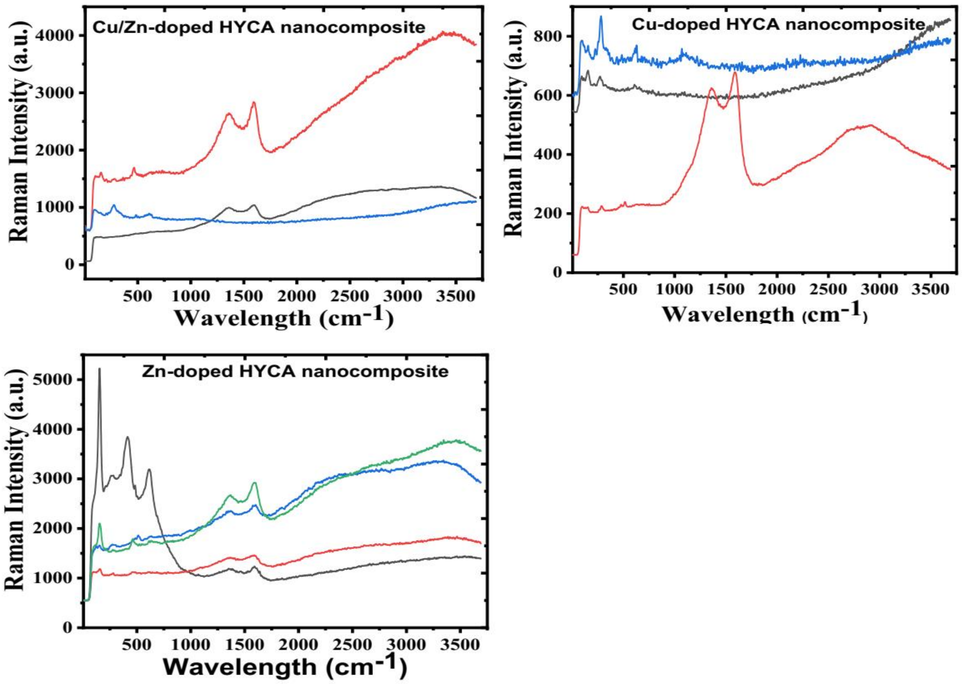

Fig. S3: Raman spectra of *Carica Papaya* seeds, Kaolinite clay, Cu/Zn-doped, Cu-doped and Zn-doped hybrid clay nanocomposites.

6.0 Energy Dispersive X-Ray Analysis

The absence of Al in Cu-doped nanocomposite could explain why it is the least efficient material for disinfection of *E. coli* in water compared to the other two composites[4]. All three nanocomposites contain Cl from the transition metal salts used in their preparation. Chemical elements such as Fe and Ca could be regarded as 'impurities' present in Kaolinite mineral even though Fe is present in *Carica papaya* seeds which explains its higher amount in the composites [5]**.** The increased carbon content in the nanocomposites when compared with raw Kaolinite is traceable to *Carica papaya* seeds used in the preparation of the nanocomposites. Both transition metals used in doping were found in the respective nanocomposites. Cu appears in the Zn-doped nanocomposite due to impurities from the Zn salt used in preparing the nanocomposite.

Table S2: Energy Dispersive X-Ray (EDX) Analysis For Raw Kaolinite, *Carica Papaya* Seed, Zn-doped, Cu-doped And Cu/Zn-doped Nanocomposites

Element	*Kaolinite (wt%)	+Zn-doped HYCA (wt%)	+Cu-doped HYCA (wt%)	+Cu/Zn-doped HYCA (wt%)
C	14.08	36.44	20.86	25.32
O	55.91	33.04	23.02	13.88
Mg	-	0.54	-	-
Al	15.25	6.27	0.41	2.79
Si	14.51	10.10	0.47	8.83
Cl	-	1.63	11.04	5.52
K		0.23	-	0.23
Ca		0.39	-	
Ti		1.03	-	0.51
Cr	-	-	-	0.26
Fe	0.25	0.86	0.90	2.26
Cu		1.89	43.31	30.59
Zn	-	7.58	-	9.80

- not detected

**Sample was carbon-coated*

+ Sample was Au-coated

7.0 High Resolution Transmission Electron Microscopy

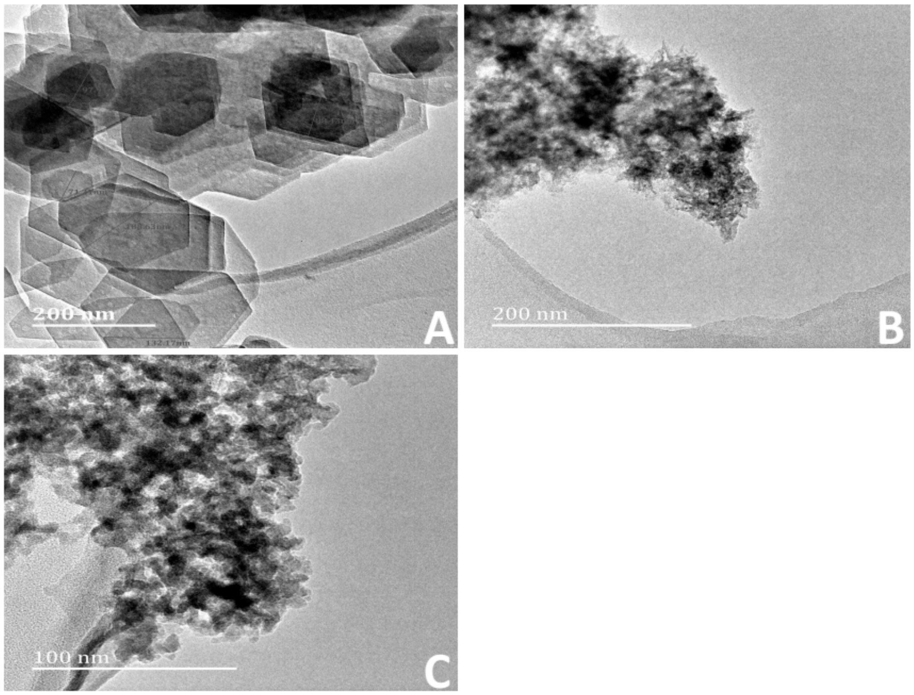

Fig. S4: High Resolution Transmission Electron Microscopy Images of (A) Kaolinite clay (B) Cu/Zn-doped nanocomposite @ 200 nm and (C) Cu/Zn-doped nanocomposite @ 100 nm.

8.0 Breakthrough Times

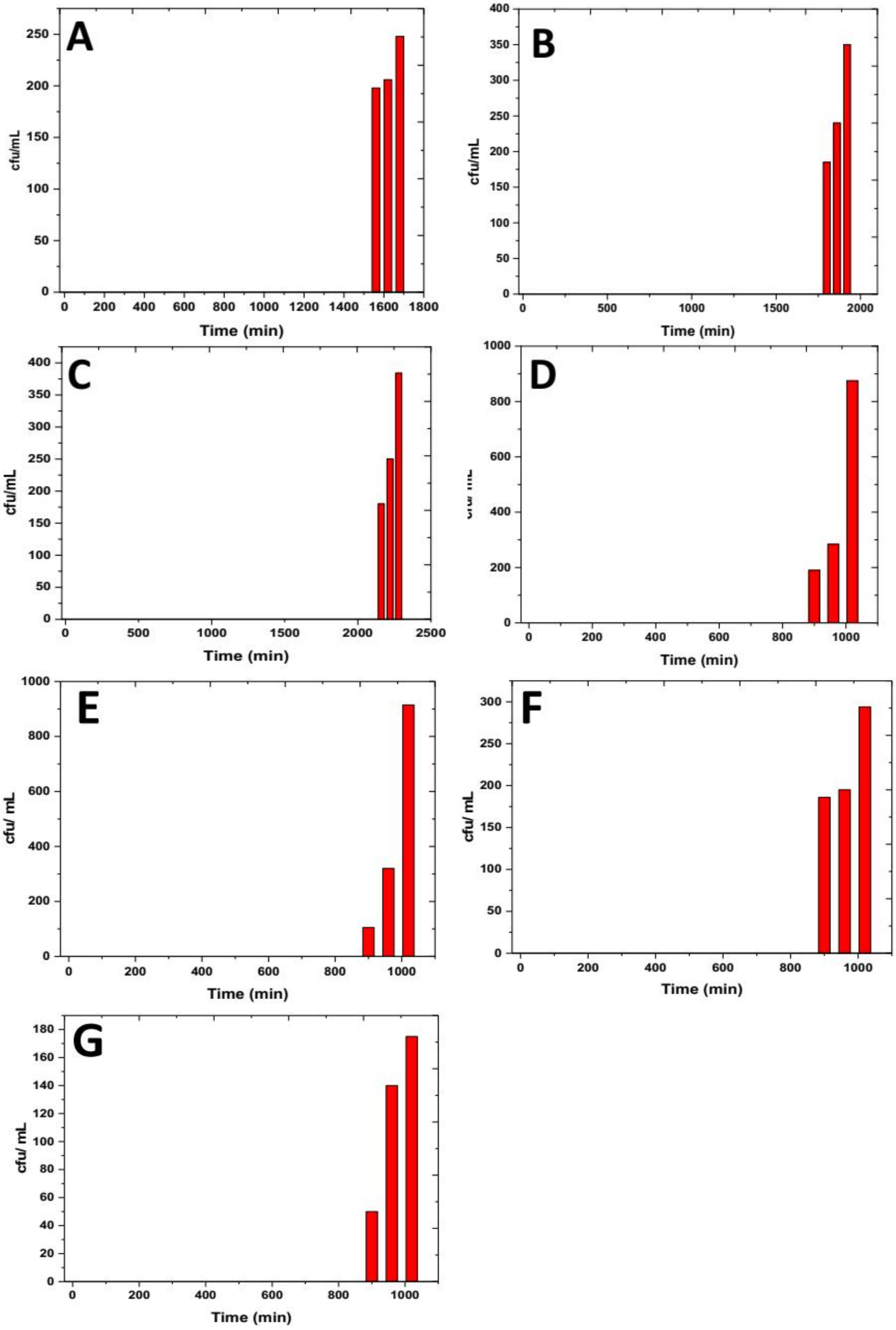

Fig. S5: Breakthrough plots for the removal of *E. coli* ATCC 29522 from water using ambient illumination in the laboratory for (A) Zn-doped HYCA (B) Cu-doped HYCA (C) Cu/Zn-doped HYCA composite adsorbents. Water disinfection of Cu/Zn-doped HYCA composite adsorbents for (D) EC_6 MDR *E. coli* (E) EC_4 MD-MMR *E. coli* (F) $EC_6 + EC_4$ MD-MMR *E. coli* (G) EC_6 MD-MMR *E. coli* + *E. coli* ATCC 29522

9.0 Dark Experiment

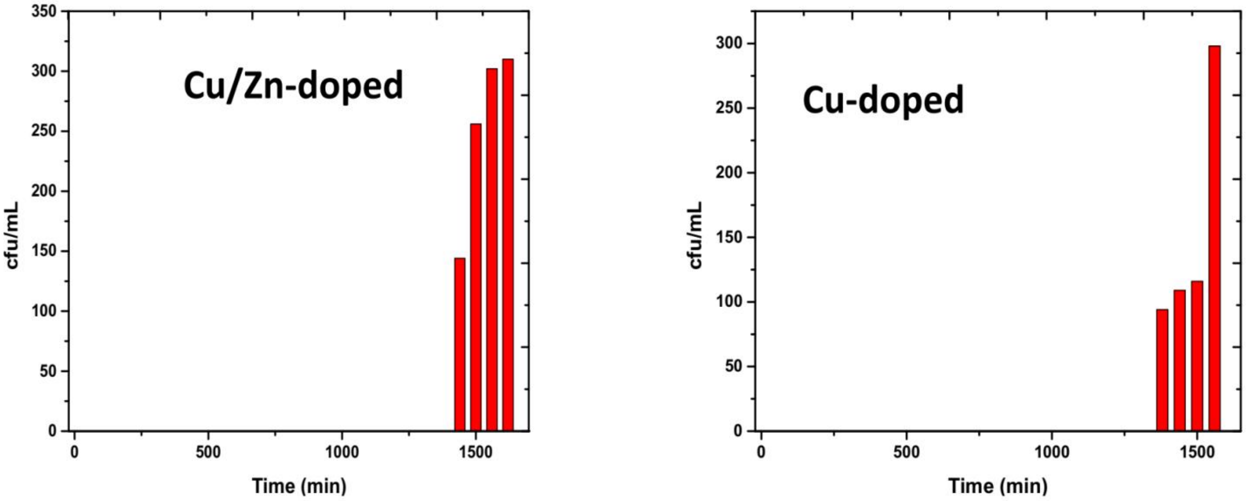

Fig. S6: Breakthrough plots for the removal of *E. coli* ATCC 29522 from water in dark conditions for Cu/Zn-doped and Cu-doped HYCA nanocomposite adsorbents

10.0 Fluorescence Spectroscopy Analysis

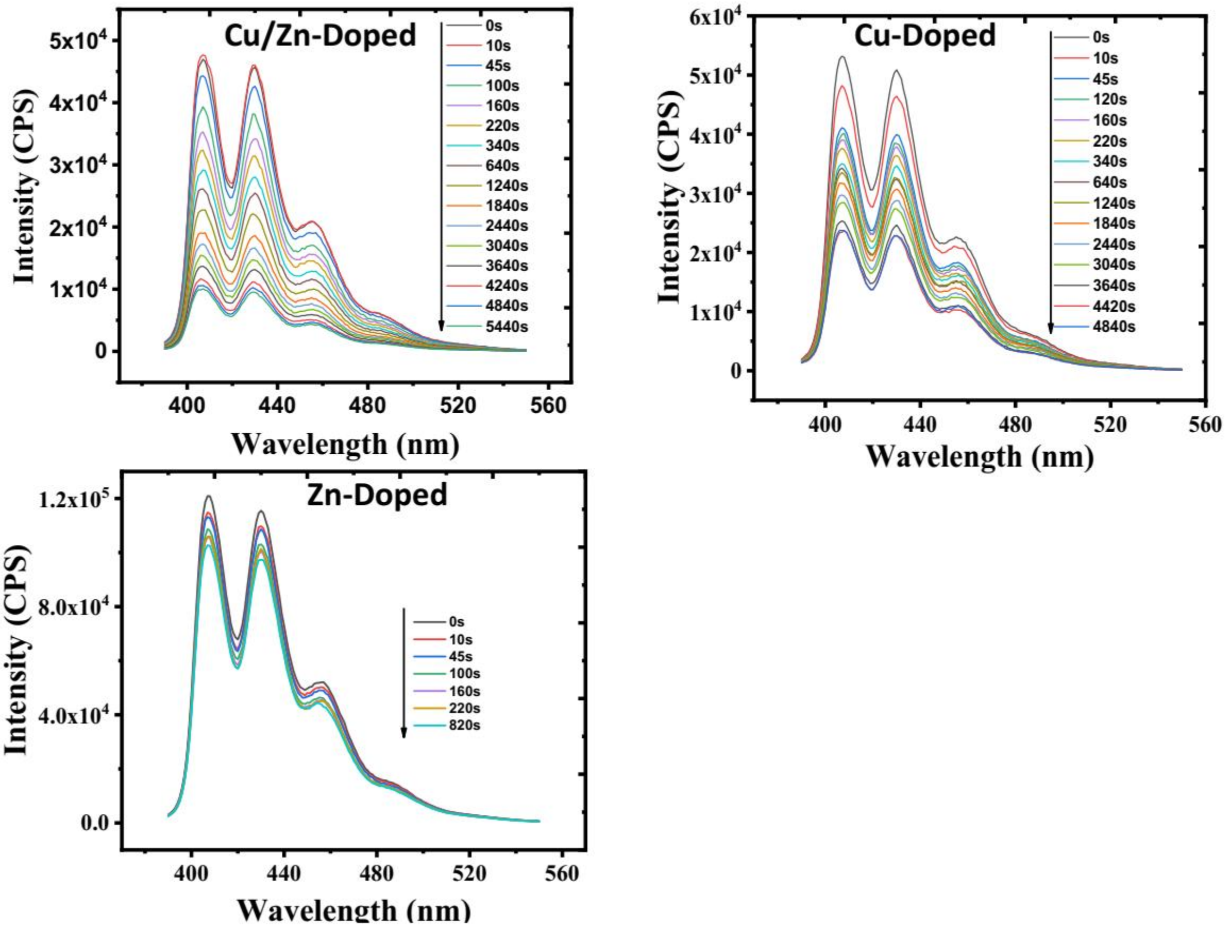

Fig. S7: Fluorescence spectra of the probe ABMDMA mixed with Cu/Zn-doped, Cu-doped and Zn-doped hybrid clay nanocomposites as a function of different exposure times of the solutions to the ambient illumination in the laboratory.

Reference

1. H. O. AbdulAziz, M. Aminu and D. A. Machido, *American Journal of Food Science and Technology*, 2016, **4**, 125-128.
2. N. Korrapati, P. S. Rao and A. V. Vinod, *Journal of Microbial and Biochemical Technology*, 2010, **2**, 74-76.
3. J. B. Patel, *Performance standards for antimicrobial susceptibility testing*, Clinical and Laboratory Standards Institute, 2017.
4. J.-K. Kang, C.-G. Lee, J.-A. Park, S.-B. Kim, N.-C. Choi and S.-J. Park, *Environmental Technology*, 2013, **34**, 703-710.
5. J. K. Peter, Y. Kumar, P. Pandey and H. Masih, *J. Pharm. Biol. Sci*, 2014, **9**, 29-37.
6. E. I. Unuabonah, C. Günter, J. Weber, S. Lubahn and A. Taubert, *ACS Sustainable Chemistry & Engineering*, 2013, **1**, 966-973.